Author/s:
Camobreco, CJ;Endrikat, S;García-Mayoral, R;Luhar, M;Chung, D

Title:
Why do only some riblets promote spanwise rollers?

Date:
2025

Citation:
Camobreco, C. J., Endrikat, S., García-Mayoral, R., Luhar, M. & Chung, D. (2025). Why do only some riblets promote spanwise rollers?. Journal of Fluid Mechanics, 1022, https://doi.org/10.1017/jfm.2025.10790.

Persistent Link:
https://hdl.handle.net/11343/367284

*J. Fluid Mech.* (2025), *vol.* 1022, A35, doi:10.1017/jfm.2025.10790

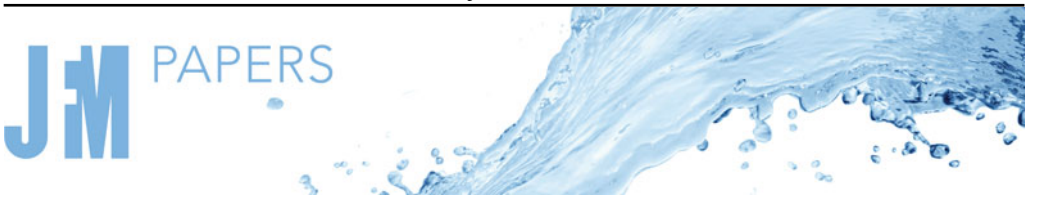

# Why do only some riblets promote spanwise rollers?

**Christopher J. Camobreco**[1], **Sebastian Endrikat**[1], **Ricardo García-Mayoral**[2], **Mitul Luhar**[3] **and Daniel Chung**[1]

[1]Department of Mechanical Engineering, University of Melbourne, Victoria 3010, Australia

[2]Department of Engineering, University of Cambridge, Cambridge CB2 1PZ, UK

[3]Department of Aerospace and Mechanical Engineering, University of Southern California, Los Angeles, CA 90089, USA

**Corresponding author:** Christopher J. Camobreco, christopher.camobreco@unimelb.edu.au

(Received 28 March 2025; revised 17 July 2025; accepted 30 September 2025)

Linear-stability modelling suggests that all sufficiently large riblets promote maximally growing spanwise rollers (García-Mayoral & Jiménez 2011 *J. Fluid Mech.* vol. 678, 317–347), yet direct numerical simulations (DNS) have shown that this is not the case (Endrikat *et al.* 2021 *J. Fluid Mech.* vol. 913, A37) some riblet shapes do not form spanwise rollers at all. Thus, the drag-reduction breakdown across all riblet shapes cannot be solely attributed to maximally growing spanwise rollers, prompting a reappraisal of the modelling. In this paper, comparing DNS data with riblet-resolving linear-stability predictions shows that the spanwise rollers are actually marginal modes, not maximally growing instabilities. This riblet-resolved linear analysis also predicts that not all riblet shapes promote spanwise rollers, in agreement with DNS, and unlike earlier linear-stability modelling, which relied on a one-dimensional (1-D) mean flow and on an over-simplified effective wall-admittance boundary condition. These riblet-resolved calculations further inform how to capture the effect of the riblet shape in a 1D model. Once captured, predictions with an effective boundary condition match riblet-resolved results, but still do not indicate what features of the riblet geometry promote the roller instability. Thus, the wall admittance is measured near the riblet crests, in both the riblet-resolved linear analysis and DNS, to show that the in-groove dynamics is dominated by a balance between the overlying pressure and unsteady inertia, and not viscous diffusion, as previously assumed. This pressure–unsteady-inertia balance sets the linear scaling of the wall admittance with riblet size, as observed in DNS, and is a key factor in setting the streamwise wavelength of the spanwise rollers. Furthermore, modelling this pressure–unsteady-inertia balance in the wall admittance reveals the role of riblet slenderness in promoting spanwise rollers,

which provides the missing link in previous correlations between the riblet geometry and the presence or lack of rollers.

**Key words:** drag reduction, turbulent boundary layers, shear-flow instability

## 1. Introduction

### 1.1. *Background*

Interest in spanwise-coherent Kelvin–Helmholtz-like rollers stems from their formation over a range of non-smooth surfaces, examples including riblets (García-Mayoral & Jiménez 2011*b*; Endrikat *et al.* 2021*a*,*b*), permeable substrates (Jiménez *et al.* 2001; Breugem, Boersma & Uittenbogaard 2006; Gómez-de-Segura *et al.* 2018*b*; Suga *et al.* 2018; Gómez-de-Segura & García-Mayoral 2019; Motoki *et al.* 2022; Habibi Khorasani, Luhar & Bagheri 2024) and plant canopies (Raupach, Finnigan & Brunei 1996; Finnigan 2000; Nepf *et al.* 2007; Ghisalberti 2009; Nepf 2012; Sharma & García-Mayoral 2020). Understanding how and why spanwise rollers form motivates this work, given that permeable substrates and engineered rough surfaces, which are susceptible to rollers, hold the potential to reduce drag, enhance heat transfer and suppress noise (García-Mayoral & Jiménez 2011*b*; Gómez-de-Segura *et al.* 2018*b*; Endrikat *et al.* 2021*a*; Kuwata 2022; Rouhi *et al.* 2022; Hartog *et al.* 2024). For these surface textures, spanwise rollers are generated by a velocity difference across the interface between the fluid region and the effectively porous fluid–solid region, where this velocity difference feeds perturbation energy production (Jiménez *et al.* 2001; García-Mayoral & Jiménez 2011*b*). The finer details of the surface texture tend to influence the appearance and intensity of the spanwise rollers, not only through the mean shear at the interface, but also through the effective wall-normal permeability of the surface texture (Endrikat *et al.* 2021*a*). In addition, the wall-normal permeability experienced by turbulent structures tends to depend on their characteristic lengths in the streamwise and spanwise directions (Gómez-de-Segura *et al.* 2018*b*; Chavarin *et al.* 2021; Endrikat *et al.* 2021*a*; Hao & García-Mayoral 2025). This turbulent-scale dependence can then lead to rollers which are either (i) flow structures which extend no further than the buffer layer ($z^+ \lesssim 50$), and which are viscous-scaled through their localisation about the local maximum of $-\partial_{zz}U^+$ (García-Mayoral & Jiménez 2011*b*, 2012), where $z$ is the wall-normal height, $U$ the mean streamwise velocity and where the superscript $()^+$ denotes normalisation by the friction velocity $u_\tau$ and kinematic viscosity $\nu$, or (ii) flow structures which extend the full height of the domain $z \lesssim \delta$, where $\delta$ is the domain height (Jiménez *et al.* 2001; Kuwata 2022; Motoki *et al.* 2022). Near-wall/buffer-layer rollers are often observed over streamwise-aligned riblets, permeable substrates (Gómez-de-Segura *et al.* 2018*b*; Habibi Khorasani *et al.* 2024) and dense filament canopies (Sharma & García-Mayoral 2020), and are the focus of this work, although with scope limited only to riblets.

For riblets, linear-stability modelling predicts that rollers form only once the effective wall admittance (the ratio of wall-normal velocity and pressure fluctuations) provided by the riblets exceeds some threshold. This effective wall admittance can be estimated from a Stokes-flow problem within the riblet grooves (García-Mayoral & Jiménez 2011*b*), and was further shown to be related to the square-root of groove area $\ell_g^+$ for conventional riblets (García-Mayoral & Jiménez 2011*b*). For riblets, $\ell_g^+$ has also been shown to reduce the scatter in the drag-reduction curves measured across different shapes, including the point of maximum drag reduction at $\ell_g^+ \approx 11$ (García-Mayoral & Jiménez 2011*a*,*b*). This relationship between linearly unstable spanwise rollers and the effective wall admittance

of the riblets thereby appeared to both explain the improved collapse of the drag-reduction curves and identify the point of maximum drag reduction. However, this roller–wall-admittance relationship was not supported by the direct numerical simulations (DNS) of Endrikat *et al.* (2021*a*), who showed that at matched $\ell_g^+$, some riblet shapes formed spanwise-coherent rollers, but others did not. Endrikat *et al.* (2021*a*) further showed that spanwise rollers were not the only contribution to the drag-reduction breakdown for riblets, as previously thought. Thus, a complete description of the drag breakdown remains an open question (Modesti *et al.* 2021; Chan *et al.* 2023; Viggiano *et al.* 2024), such that the optimal riblet size of $\ell_g^+ \approx 11$ can only be identified empirically.

### 1.2. *Outline*

This paper reconciles previous inconsistencies between linear predictions and DNS observations of spanwise rollers. This is achieved by improving our dynamical understanding of spanwise rollers based on two hypotheses. First, that the rollers are actually marginal instabilities. Second, that the emergence of rollers is driven by a balance between the unsteady term and pressure gradient within the riblet grooves, which depends on riblet slenderness. This is contrary to the existing assumption that the dynamics within the groove were dictated by a balance between the pressure gradient and viscous term. These hypotheses are verified by performing two-dimensional (2-D) riblet-resolved linear-stability analysis and further supported by new analysis of an existing DNS database (Endrikat *et al.* 2021*a*,*b*; Wong *et al.* 2024). A simpler, empirical one-dimensional (1-D) model is also developed, based on these hypotheses and the 2-D analysis, to rapidly predict many of the key characteristics of the spanwise rollers. The empirical boundary condition provides useful insights for riblet sizes up to and slightly beyond their design point (of maximum drag reduction), although the 1-D model eventually breaks down for larger riblets (earlier than its 2-D counterpart). The formal homogenisation procedure required to obtain a more rigorous 1-D boundary condition is, however, shown to be more expensive than performing the 2-D linear-stability analysis in its stead, such that the 2-D analysis forms a valuable design tool for a more refined riblet-shape optimisation.

First, § 2 presents further evidence that four of the six riblet shapes tested in Endrikat *et al.* (2021*a*) (see table 1) do not promote strong spanwise rollers, quantified by a near-zero roller drag penalty. However, a range of instantaneous flow visualisations (Chu & Karniadakis 1993; Goldstein, Handler & Sirovich 1995; Endrikat *et al.* 2021*a*,*b*; Rouhi *et al.* 2022) suggest that weak rollers persist, at least for some of these riblet shapes. Section 2 thereby establishes a more sensitive gauge of roller intensity across riblet shapes and sizes, from new analysis of minimal-channel riblet DNS data (Endrikat *et al.* 2021*a*; Modesti *et al.* 2021; Wong *et al.* 2024), as generating new DNS data was not required. Details for almost all cases in the DNS dataset, and riblet geometric parameters, are tabulated in Wong *et al.* (2024); details for the remainder of the DNS cases (for the largest $\ell_g^+$ riblets) can be found in Endrikat *et al.* (2021*a*). Overall, this more sensitive measure of roller intensity, based on the pressure fluctuation $\langle p'p' \rangle$ profiles, enables a more detailed appraisal of the linear-stability analysis in § 3, even for those riblet shapes which have roller drag penalties lying within numerical tolerances (Endrikat *et al.* 2021*a*).

Section 3 also reconsiders the wall-admittance threshold for spanwise rollers. The DNS measurements of Endrikat *et al.* (2021*a*, figure 13*b*) showed that crest-measured wall admittances for riblets are $\hat{w}^+/\hat{p}^+ \approx 0.02$ to $\approx 0.03$ when rollers begin to appear ($\ell_g^+ \approx 10$ to 15), where $w$ is the wall-normal velocity, $\hat{w}$ its Fourier transform, $p$ is the pressure, and where $\hat{w}^+/\hat{p}^+$ was integrated across all wavelengths $\lambda_y^+ \gtrsim 250$ and $65 \lesssim \lambda_x^+ \lesssim 290$. Note $x$ is the streamwise, $y$ the spanwise and $z$ the wall-normal coordinate. However, at

| | Blade | Trapezoid | 30° Triangle |
|---|---|---|---|
| Shape: | 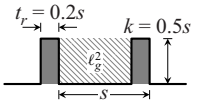  | 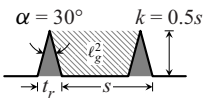  | 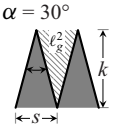  |
| Groove sizes tested, $\ell_g^+$ | 4.9, 7.5, 9.9, 12.8 15.8, 21.1, 24.7, 31.0 | 5.0, 7.5, 9.7, 11.8 15.0, 20.6, 24.0, 32.9, 41.1 | 7.5, 9.8, 12.1, 20.4 |
| Roller drag penalty | Small, past $\ell_g^+ \gtrsim 13$ | Negligible, all $\ell_g^+$ | Appreciable, past $\ell_g^+ \gtrsim 10$ |
| | 60° Triangle | 90° Triangle | Asymmetric triangle |
| Shape: | 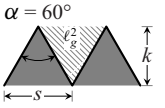  | 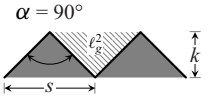  | 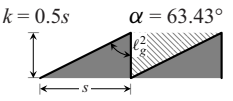  |
| Groove sizes tested, $\ell_g^+$ | 7.5, 9.7, 11.8, 23.0 | 5.0, 7.4, 9.6, 12.5, 25.0 | 5.0, 7.4, 9.6 11.4, 15.6, 20.8 |
| Roller drag penalty | Negligible, all $\ell_g^+$ | Negligible, all $\ell_g^+$ | Negligible, all $\ell_g^+$ |

Table 1. Six of the riblet shapes considered in past minimal-channel DNS (Endrikat *et al.* 2021*a*; Modesti *et al.* 2021; Wong *et al.* 2024), their corresponding geometric parameters (spanwise spacing $s$, height $k$, tip-angle $\alpha$, base thickness $t_r$, square-root of groove area $\ell_g$) and the viscous-scaled square-root of groove areas at which past DNS were conducted. Whether a drag penalty was attributed to spanwise rollers forming over the riblets (Endrikat *et al.* 2021*a*, figure 11*b*) is also listed for each shape.

$\ell_g^+ \approx 10$ to 15, the wall admittance of the model boundary condition of García-Mayoral & Jiménez (2011*b*) was 5–10 times higher than DNS measurements (Endrikat *et al.* 2021*a*), i.e. $\hat{w}^+/\hat{p}^+ \approx 0.1$ to $\approx 0.3$, integrated across the same $\lambda_x^+$ and $\lambda_y^+$ ranges. Indeed, these $\hat{w}^+/\hat{p}^+ \gtrsim 0.1$ model-predicted roller modes shared many of the characteristics of the maximally growing Kelvin–Helmholtz-like rollers which form in the free-shear-layer limit (García-Mayoral & Jiménez 2011*b*, comparing figures 19*c* and 19*e*), and notably, had streamwise wavelengths of $\lambda_x^+ \approx 60$, rather than $\lambda_x^+ \approx 150$ as measured for rollers over riblets in DNS (García-Mayoral & Jiménez 2011*b*; Endrikat *et al.* 2021*a*). Separately, the 2-D resolvent analysis of Chavarin & Luhar (2020) found spanwise roller modes with high relative gains at a streamwise wavelength ($\lambda_x^+ \approx 130$) similar to DNS for $\ell_g^+ \approx 13$ blade riblets, by essentially assuming zero growth (marginal) modes. Marginal modes are zero-growth-rate modes for a given $\ell_g^+$, $\lambda_x^+$ combination, where a change in either $\ell_g^+$ or $\lambda_x^+$ results in the growth rate of the mode switching sign (unlike neutral modes, across which the growth rate does not switch sign), following the definition in Drazin & Reid (2004). In summary, these results suggest that rollers over riblets are not maximally growing instabilities. Comparison between riblet-resolved linear-stability predictions and DNS data in § 3 confirms that rollers over riblets are not maximally growing. Instead, they are marginally stable structures emerging at lower wall-admittance values, a conclusion which is further verified by the linear-stability analysis accurately predicting key characteristics (streamwise wavelengths and wave speeds) of the spanwise rollers.

After further showing that only some riblet shapes promote these marginal rollers, the question then turns to explaining why. In Endrikat *et al.* (2021*a*), the sustenance of spanwise rollers was well correlated with high momentum absorption near the riblet crests, and not the effective riblet wall admittance alone. This conclusion is supported in § 4, as riblet-resolved linear-stability predictions of rollers prove sensitive to some of the details of the mean-velocity profile within the grooves, where the mean profile encapsulates the momentum absorption near the crest plane. The effective wall-admittance boundary

condition is also reconsidered, in an effort to develop an improved dynamical model to predict roller formation. Previously, the wall admittance was assumed proportional to riblet size and streamwise scale, as $\hat{w}^+/\hat{p}^+ \propto \ell_g^{+3}\lambda_x^{+-2}$ (García-Mayoral & Jiménez 2011*b*), where $\lambda_x$ is the streamwise wavelength; separately, for permeable substrates, a streamwise-scale-independent model boundary condition $\hat{w}^+/\hat{p}^+ \propto$ constant has been assumed (Jiménez *et al.* 2001; Motoki *et al.* 2022). However, § 4 shows that the wall admittance provided by riblets does not vary as $\hat{w}^+/\hat{p}^+ \propto \lambda_x^{+-2}$, as the dominant balance near the riblet crests is not between viscous diffusion and overlying pressure. Assuming the overlying pressure is instead balanced by unsteady in-groove inertia near the crests both explains the trends in the DNS measurements (Endrikat *et al.* 2021*a*) and corrects the streamwise-scale dependence of the wall-admittance model to $\hat{w}^+/\hat{p}^+ \propto \lambda_x^{+-1}$.

Section 5 tests this understanding of the improved wall-admittance boundary condition with 1-D linear-stability analysis. This linear analysis provides reasonable predictions of the streamwise wavelengths and wave speeds of rollers at their onset, but eventually suggests large ($\ell_g^+ \gtrsim 25$) 90° triangular ◢◣◢◣ and asymmetric triangular ◢◢◣ riblets would sustain rollers, unlike the riblet-resolved analysis and DNS. Accurately modelling not only the wall admittance but also the streamwise slip is required for larger riblets. Finally, conclusions are provided in § 6.

## 2. Identifying rollers over riblets from DNS

The aim of this section is to develop a more sensitive measure of the intensity of spanwise rollers forming over riblets, so as to provide a more detailed comparison between DNS and linear-stability analysis. Endrikat *et al.* (2021*a*) identified strong rollers for blade ▯▯▯ and 30° triangular ◢◣◢◣ riblets by measuring a roller drag penalty $0.1 \lesssim \Delta U_{KH}^+ \lesssim 0.5$. The roller drag penalty $\Delta U_{KH}^+$ is a measure of the change in drag produced by a difference in Reynolds stresses between smooth and riblet surfaces for large spanwise-wavelength Fourier modes. This measure was calculated following the procedure in MacDonald *et al.* (2016), similar to García-Mayoral & Jiménez (2011*b*), except (i) integrated in spectral space across $65 \lesssim \lambda_x^+ \lesssim 290$, $250 \lesssim \lambda_y^+ \lesssim \infty$ and for $0 \leqslant z^+ \lesssim 100$ and (ii) neglecting any $z^+$ where the $\lambda_x^+$, $\lambda_y^+$ integrated Reynolds stresses over the riblet are negative. Weak rollers, with $\Delta U_{KH}^+ \approx 0$, were still suggested by visualisations of the instantaneous wall-shear stress for the remaining riblet shapes. Similar visualisations are provided in figure 1. Following Endrikat *et al.* (2021*a*) and Rouhi *et al.* (2022), the (instantaneous) presence of rollers over riblets can be inferred from regions of high negative wall-shear stress or wall pressure which are approximately spanwise uniform. Strong rollers form over 30° triangular ◢◣◢◣ riblets, as indicated by spanwise-coherent regions of negative wall-shear stress and (phase-shifted) spanwise-coherent regions of wall pressure. Weaker rollers are suggested for blade ▯▯▯, 30° trapezoidal ▯▯▯ and 60° triangular ◢◣◢◣ riblets, with both reduced spanwise coherence, and fewer rollers overall. Rollers become almost non-existent for 90° triangular ◢◣◢◣ and asymmetric triangular ◢◢◣ riblets, with almost no negative wall-shear stress events (for this threshold), although the wall pressure may still indicate the presence of one or two weak rollers. Overall, while an accurate measure of the drag penalty of these rollers may still be $\Delta U_{KH}^+ \approx 0$, $\Delta U_{KH}^+$ is sensitive to both the choice of turbulence origin $\ell_T^+$ and *ad hoc* cutoffs in spectral space. Thus, an alternative gauge of roller intensity is sought.

Spectral signatures of the rollers, which could quantify their intensity, are also present in almost all near-wall measurements of fluctuation products, e.g. $\hat{u}'\hat{u}'$, $\hat{v}'\hat{v}'$, $\hat{w}'\hat{w}'$,

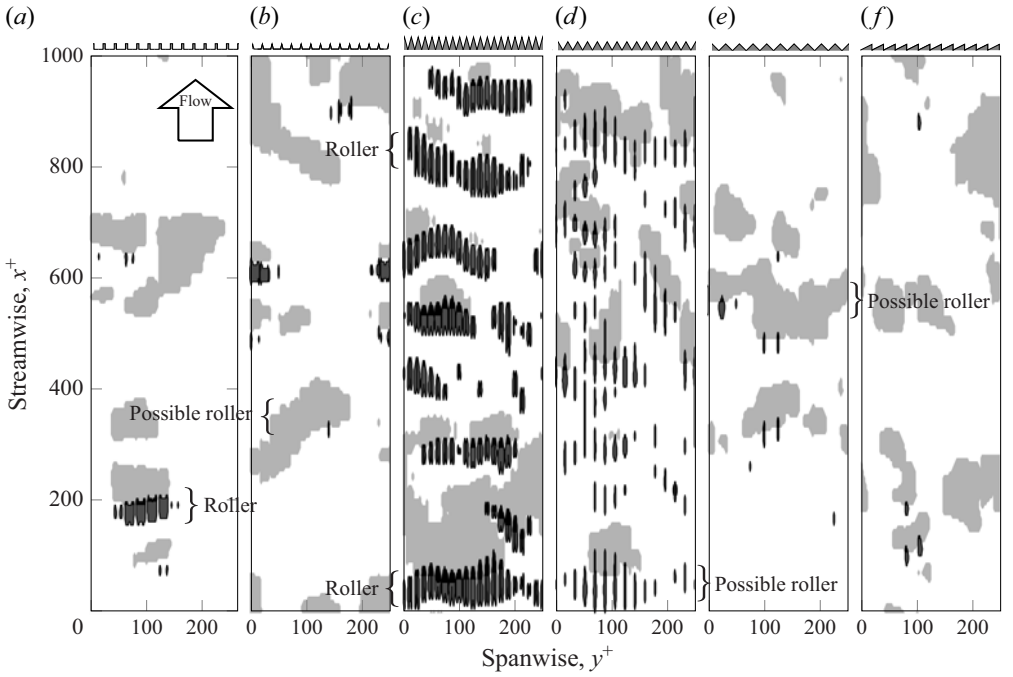


Figure 1. Plan view of spanwise rollers via the instantaneous wall-shear stress (black) and the excess instantaneous wall pressure (grey) for $\ell_g^+ \approx 12$ riblets of various shapes. The threshold for the wall-shear stress is $\tau^+ = -0.2$, as in Endrikat *et al.* (2021*b*), while the threshold for the excess instantaneous wall pressure is $p^+ - \langle p^+ \rangle_{x_r, y_r} = -2$; here $\langle \cdot \rangle_{x_r, y_r}$ indicates averaging across all points on the riblet surface.

$\hat{u}'\hat{w}'$, $\hat{p}'\hat{p}'$ (García-Mayoral & Jiménez 2011*b*; Endrikat *et al.* 2021*a*,*b*), where $u$ is the streamwise velocity, $v$ the spanwise velocity and where the superscript $()'$ denotes a fluctuation. Of these, the spectra of $\hat{p}'\hat{p}'$ seem to be the most uniform in the wall-normal direction (MacDonald *et al.* 2017), minimising the issue of an ambiguous $\ell_T^+$. Equally, flow visualisations have shown $p'$ maintains spanwise coherence even well below the interface of a porous substrate (Habibi Khorasani *et al.* 2024). Thus, the magnitude of the time- and spanwise-averaged $\langle p'p' \rangle$ profiles are considered figure 2 for each riblet shape, intrinsically averaged below the riblet crests. From figure 2, it is readily apparent that rollers are promoted by some riblet shapes, e.g. 30° triangular riblets especially (figure 2*c*), given the increase in $\langle p'p' \rangle$ relative to its smooth-wall counterpart.

Based on the results of figure 2, the intensity of the spanwise rollers is quantified by $\max(\langle p'p' \rangle^+)/\max(\langle p'_{sm} p'_{sm} \rangle^+)$, taking the maxima across all $z^+$, and where $p'_{sm}$ is the pressure fluctuation over a smooth wall. These intensities are collected for each of the riblet shapes and plotted as a function of $\ell_g^+$ in figure 3(*a*). If the threshold for sustaining rollers were at some fixed $\ell_g^+$, all these intensities would increase in concert, regardless of riblet shape, say, at $\ell_g^+ \approx 11$. However, as shown in figure 3(*a*), the roller intensity increases for the 30° triangular riblets at $\ell_g^+ \approx 11$, but is delayed slightly for some of the other riblet geometries, e.g. the blade riblets at $\ell_g^+ \approx 13$, consistent with the prediction for similar blade riblets in the 2-D resolvent analysis of Chavarin & Luhar (2020). Equally, the intensities of rollers varies greatly with riblet shape (figure 3*a*). The highest intensities are attained with 30° triangular riblets, with $\max(\langle p'p' \rangle^+)/\max(\langle p'_{sm} p'_{sm} \rangle^+)$ reaching $\approx 3$, followed by blades, 30° trapezoidal and 60° triangular riblets

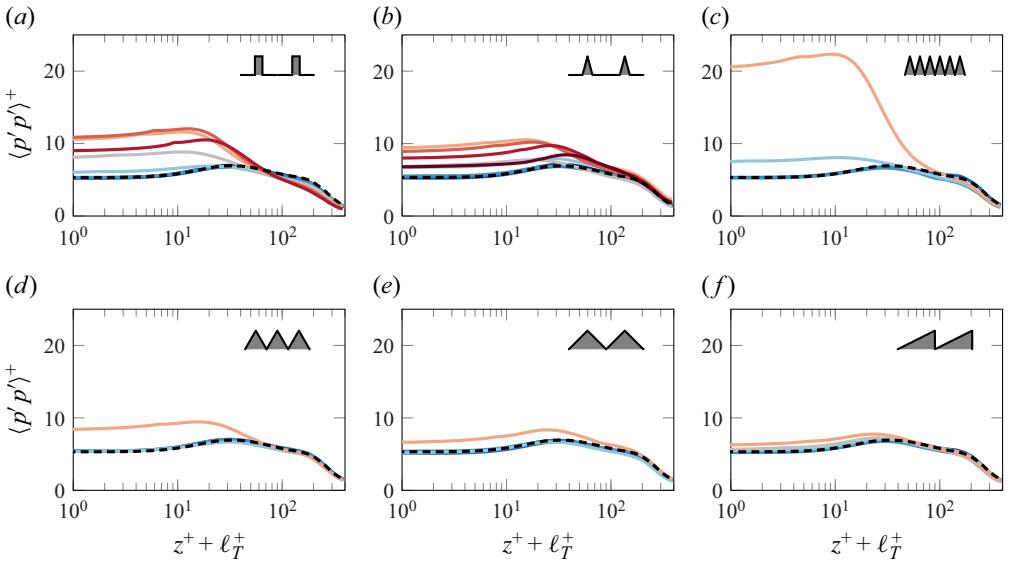


Figure 2. Time- and plane-averaged $\langle p'p'\rangle^+$ profiles for riblets (solid coloured) and a smooth wall (dashed black), having reprocessed the DNS datasets of Endrikat *et al.* (2021*a*), Modesti *et al.* (2021) and Wong *et al.* (2024), and intrinsically averaging below the crests. The magnitude of $\langle p'p'\rangle^+$ relative to that over a smooth wall gives an indication of the presence (or lack) of spanwise rollers. The diverging blue-grey-red colour scheme indicates the riblet size (blue smallest $\ell_g^+$, red largest), where matched colours between panels represent approximately matched $\ell_g^+$ riblets.

with increasingly reduced intensities. For blade ⊓⊓ and 30° trapezoidal ⩚ riblets, the roller intensities peak at $\ell_g^+ \approx 20$ to 25. For even larger riblets, $\ell_g^+ \gtrsim 40$, this measure of the roller intensity then drops, with $\max(\langle p'p'\rangle^+)/\max(\langle p'_{sm}p'_{sm}\rangle^+)$ tending back toward unity, and hinting at a weakening of the roller mode as the riblet spacing increases. These minimal-channel DNS results are consistent with the recent experiments of Abu Rowin *et al.* (2025), who also showed that rollers weaken for slender triangular riblets at $\ell_g^+ \gtrsim 40$.

When rollers form, not only does the intensity of $\langle p'p'\rangle^+$ increase (figure 3*a*), but the peak pressure of the 2-D cospectra of $\hat{p}'\hat{p}'$ also shifts from $\lambda_x^+ \approx 200$ to $\lambda_x^+ \approx 150$. This was shown for blade ⊓⊓ riblets in García-Mayoral & Jiménez (2011*b*) and for 30° triangular ⩚⩚ riblets in Endrikat *et al.* (2021*b*). Thus, slices of the 2-D cospectra of $\hat{p}'\hat{p}'$ are shown in Appendix A, figure 10 at $z^+ + \ell_T^+ \approx 10$ for all riblet sizes and shapes for which the roller intensity was measured in figure 3(*a*). From these cospectra, the streamwise wavelengths of the peak pressure are collected in figure 3(*b*). Between $\ell_g^+ \approx 11$ to $\ell_g^+ \approx 13$, the shift in peak pressure from $\lambda_x^+ \approx 200$ to $\lambda_x^+ \approx 150$ is evident for 30° triangular ⩚⩚, blade ⊓⊓ and 30° trapezoidal ⩚ riblets, indicating the appearance of spanwise rollers. However, for the remaining three riblets – 60° triangular △△, 90° triangular ⩚ and asymmetric triangular ◿◺ riblets – there is no clear shift in wavelength. Given the slightly higher roller intensities for 60° triangular △△ riblets, very weak rollers may persist for this riblet shape, while 90° triangular ⩚ and asymmetric triangular ◿◺ riblets are essentially ruled out of having rollers of any relevant intensity.

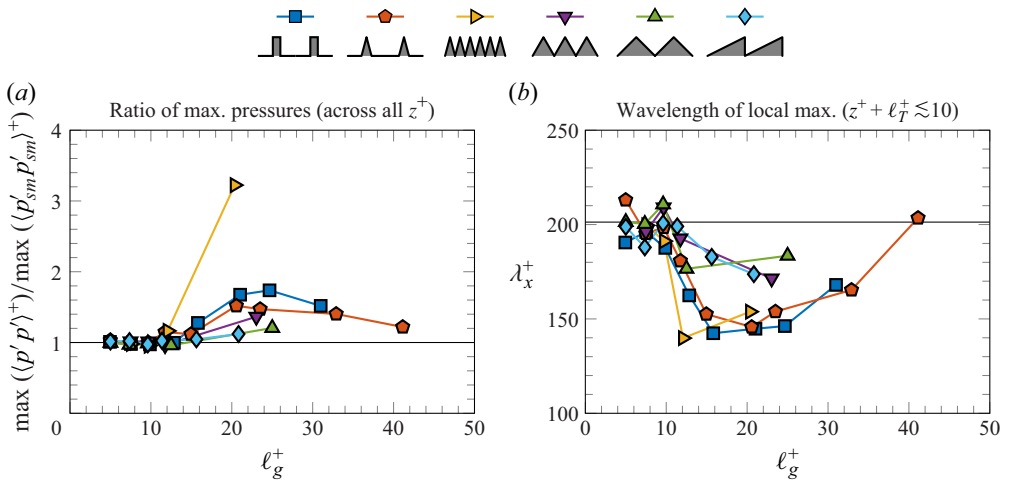


Figure 3. Identifying which riblets have rollers and gauging their intensity through (*a*) the ratio of the maximum of the $x$-$y$-$t$ averaged pressure fluctuations $\langle p'p'\rangle^+$, relative to that over a smooth wall, cf. figure 2, and (*b*) the streamwise wavelength of the local maximum in the pressure spectra (integrated across all $\lambda_y^+$ and all $z^+ + \ell_T^+ \lesssim 10$); see Appendix A for more. Thin solid black lines indicate the equivalent smooth-wall values, $\max(\langle p'p'\rangle^+)/\max(\langle p'_{sm}p'_{sm}\rangle^+) = 1$ and $\lambda_x^+ \approx 200$, respectively. Although the ratio $\max(\langle p'p'\rangle^+)/\max(\langle p'_{sm}p'_{sm}\rangle^+)$ should be approximately independent of channel size at matched $Re_\tau$, where $Re_\tau$ is the friction Reynolds number, the magnitude of $\langle p'p'\rangle$ in minimal-channel DNS is about 20 % larger near the wall than its full channel equivalent; for further discussion, see MacDonald *et al.* (2017, § 3.2).

## 3. Riblet-resolved linear-stability analysis

The question of whether spanwise rollers are actually a maximally growing instability was raised in § 1.2. Rollers were believed to be a maximally growing instability from the results of linear-stability modelling with an effective wall-admittance boundary condition (García-Mayoral & Jiménez 2011*b*), and specifically a boundary condition which was later shown to incorrectly scale with riblet size (Endrikat *et al.* 2021*a*), i.e. $\hat{w}^+/\hat{p}^+ \propto \ell_g^+$ and not $\propto \ell_g^{+3}$ as previously assumed. Thus, to avoid any uncertainties introduced by an effective wall-admittance boundary condition, the riblets are first resolved directly as a no-slip, impermeable surface in this section. The results of the riblet-resolved linear-stability analysis are then compared with DNS to show that rollers are actually near marginally stable and not maximally growing as previously believed. This linear-stability analysis then also provides a means of predicting which riblet shapes are likely to promote spanwise rollers.

### 3.1. *Methods*

Linear perturbations in the velocity and pressure are expressed as $\{\boldsymbol{u}', p'\}(x, y, z, t) = \{\hat{\boldsymbol{u}}, \hat{p}\}(y, z)\exp[\mathrm{i}(\kappa_x x + \kappa_y y - \omega t)]$, with streamwise wavenumber $\kappa_x$, spanwise wavenumber $\kappa_y$ and frequency $\omega$; again, $z$ denotes the wall-normal coordinate, and $t$ time. Focus is placed on perturbations with small spanwise wavenumber $\kappa_y$, i.e. large spanwise wavelength $\lambda_y = 2\pi/\kappa_y$, as spanwise-coherent rollers typically have $\lambda_y^+ \gtrsim 120$ (García-Mayoral & Jiménez 2011*b*; Endrikat *et al.* 2021*a*), and as suggested by the higher magnitudes of the pressure cospectra at $\lambda_y^+ \gtrsim 100$ in Appendix A. For simplicity, $\kappa_y = 0$ is considered henceforth, noting that of the other large wavelength modes tested ($\lambda_y^+ \approx 125$ and $\lambda_y^+ \approx 250$), all had higher decay rates than the spanwise-infinite ($\kappa_y = 0$) modes (Appendix B).

The perturbations satisfy the linearised Navier–Stokes equations

$$\left[-\mathrm{i}\omega^+ + U^+\mathrm{i}\kappa_x^+ + {\kappa_x^+}^2 - \partial_{yy} - \partial_{zz}\right]\hat{u}^+ + \hat{v}^+\partial_y U^+ + \hat{w}^+\partial_z U^+ = -\mathrm{i}\kappa_x^+\hat{p}^+, \tag{3.1}$$

$$\left[-\mathrm{i}\omega^+ + U^+\mathrm{i}\kappa_x^+ + {\kappa_x^+}^2 - \partial_{yy} - \partial_{zz}\right]\hat{v}^+ = -\partial_y\hat{p}^+, \tag{3.2}$$

$$\left[-\mathrm{i}\omega^+ + U^+\mathrm{i}\kappa_x^+ + {\kappa_x^+}^2 - \partial_{yy} - \partial_{zz}\right]\hat{w}^+ = -\partial_z\hat{p}^+, \tag{3.3}$$

$$\mathrm{i}\kappa_x^+\hat{u}^+ + \partial_y\hat{v}^+ + \partial_z\hat{w}^+ = 0, \tag{3.4}$$

here expressed in viscous units and having linearised about a one-component, two-dimensional mean flow $U(y, z)$. The mean flow satisfies

$$\left(1+\nu_e^+\right)\partial_{yy}U^+ + \partial_z\left[\left(1+\nu_e^+\right)\partial_z U^+\right] = 1/Re_\tau, \tag{3.5}$$

where $Re_\tau = u_\tau\delta/\nu$ is the friction Reynolds number based on a domain height $\delta$, and where the eddy viscosity $\nu_e^+$ captures the influence of the Reynolds stresses ($\overline{u'w'}$) on the mean flow. Note that eddy viscosity is applied only when obtaining the mean flow (3.5), i.e. eddy viscosity is not included in (3.1)–(3.3) when solving for the perturbations. Eddy viscosity is not overly important for accurately predicting spanwise rollers over riblets, given their near-wall location (Gómez-de-Segura 2019), and including eddy viscosity in (3.1)–(3.3) leads to only a small reduction in growth rate (figure 4*d*, comparing red solid and red dashed curves).

Boundary conditions in the spanwise direction are periodic (with period corresponding to riblet spacing $s^+$), and along the riblet wall are no-slip, on both the mean flow ($U^+ = 0$) and the perturbations ($\hat{\boldsymbol{u}} = 0$). Symmetry conditions at the channel centreline ($\partial_z U^+ = 0$, $\partial_z\hat{u}^+ = \partial_z\hat{v}^+ = w^+ = 0$) are placed at $z^+ = Re_\tau - \ell_T^+$, taking the riblet crests at $z^+ = 0$, to ensure a consistent domain height for both riblet and smooth-wall calculations, and where $\ell_T^+$ is the turbulence origin. How $\ell_T^+$ is selected for each riblet size and shape is discussed in Appendix C. A Cess profile for the eddy viscosity $\nu_{e,S}^+(z^+) = 0.5(1 + (\kappa Re_\tau(1-z'^2)(1+2z'^2)(1-\exp(-(1-|z'|)Re_\tau/A))/3)^2)^{1/2} - 0.5$ is assumed (Reynolds & Tiederman 1967), where $z' = (z^+ - Re_\tau)/Re_\tau$. The constants selected for the Cess profile (von Kármán constant $\kappa = 0.46$ and van Driest constant $A = 30.7$) minimise the sum-squared difference relative to the full-channel smooth-wall DNS mean profile of Endrikat *et al.* (2021*a*) at $Re_\tau = 395$, following Moarref & Jovanović (2012), cf. $\kappa = 0.45$, $A = 29.4$ at $Re_\tau = 547$. The eddy-viscosity profile for riblets $\nu_{e,R}$ is unchanged, except for a wall-normal shift by $\ell_T^+$, i.e. $\nu_{e,R}^+(z^+) = \nu_{e,S}^+(z^+ + \ell_T^+)$, and where $\nu_{e,R}^+(z^+) = 0$ for all $z^+ \leqslant -\ell_T^+$.

Solutions to the eigenvalue problem (3.1)–(3.4) and the mean flow (3.5) are obtained in FreeFem++ (Hecht 2012), having defined the riblet shape and grid sizes in Gmsh (Geuzaine & Remacle 2009). The meshes are unstructured, to maintain grid sizes $\Delta_y^+ \approx \Delta_z^+ \approx 0.1$ near the riblets, and $\Delta_y^+ \approx \Delta_z^+ \approx 2$ in the far-field. Based on the typical spacing of a roller-promoting riblet ($s^+ \approx 20$), these grid sizes correspond to $\approx$ 200 points per riblet spacing near the crests, and, e.g. $\approx$ 40 points across the tips of the blade ⊓⊓ riblets. The finite elements are triangular, second-order in velocity and first-order in pressure. The eigenvalue subroutine uses a shifted-inverse method, with a typical initial guess of a wave speed of $c^+ \approx 4$ (and zero growth rate), and with the nearest four eigenvalues requested to a relative tolerance of $10^{-12}$. The grid-resolution error was also assessed for trapezoidal ∧∧ riblets in the range $70 \lesssim \lambda_x^+ \lesssim 400$ (figure 4*d*, comparing red solid and black dashed curves) as relevant to spanwise rollers. The errors in the growth rate were below 0.1 % relative to halved grid sizes, $\Delta_y^+ \approx \Delta_z^+ \approx 0.05$

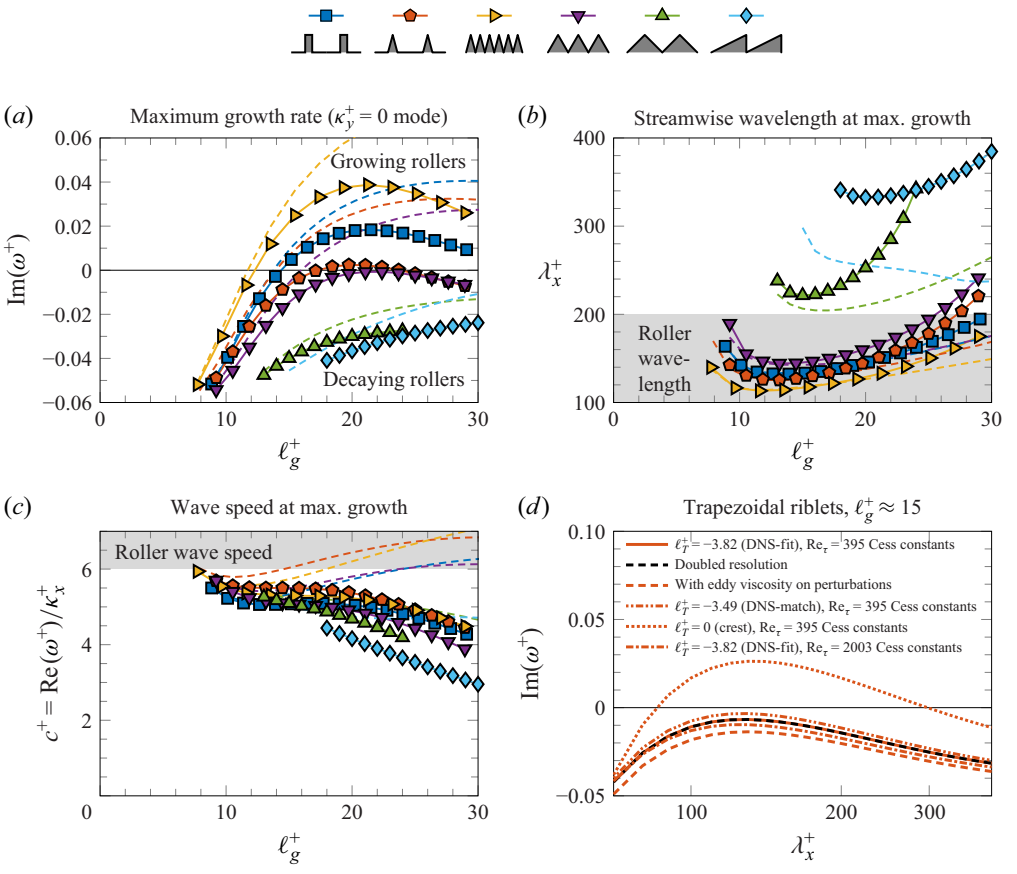


Figure 4. Predictions of the riblet-resolved linear-stability analysis for riblets with sizes $\ell_g^+ \lesssim 30$. Positive growth rates indicate growing rollers, which are not achieved by all riblet shapes. (*a*) Growth rate of the spanwise-infinite mode, at the local maximum in growth rate (only if present). (*b*) Corresponding streamwise wavelength, with the shaded region indicating typical values for rollers from DNS (García-Mayoral & Jiménez 2011*b*; Endrikat *et al.* 2021*a*). (*c*) Corresponding wave speed, with the shaded region again indicating typical values for rollers from DNS. In (*a–c*), solid lines use DNS-interpolated $\ell_T^+$ values for the Cess profile, and dashed lines use *a priori* viscous vortex model $\ell_T^+$ values. See Appendix C for more. (*d*) Assessment of the sensitivity of the growth rate predictions to the numerical resolution and to modelling assumptions. Only the choice of the turbulence origin $\ell_T^+$ proves greatly important.

near the riblets and $\Delta_y^+ \approx \Delta_z^+ \approx 1$ in the far-field; for reference, this required $\approx 1.14$ M elements, compared with $\approx 0.28$ M elements for the baseline resolution used henceforth.

### 3.2. *Predicting which riblets have rollers*

As shown in figure 4, linear-stability analysis in which the detailed riblet shapes are resolved, and not modelled with an effective boundary condition, yields predictions consistent with DNS (García-Mayoral & Jiménez 2011*b*; Endrikat *et al.* 2021*a*,*b*). This includes predicted wavelengths near $\lambda_x^+ \approx 150$ (figure 4*b*), predicted wave speeds near $c^+ \approx 6$ (figure 4*c*), and the roller mode first appearing at $\ell_g^+ \approx 10$ upon increasing $\ell_g^+$ (figure 4*a*), all consistent with DNS of rollers over riblets.

The 2-D linear-stability analysis also correctly predicts that rollers should be most intense for 30° triangular ⋀⋀⋀ riblets, as their roller growth rates are the highest across

the riblet shapes tested (figure 4*a*). In addition, rollers would be next-most intense for blade ⊓⊓, 30° trapezoidal ⩚ and then 60° triangular △△△ riblets, respectively, consistent with the DNS ordering of intensities (figure 3*a*). However, the 2-D linear-stability analysis differs slightly from the DNS in terms of when rollers first become marginal. For example, from DNS measurements (figure 3), rollers are expected at $\ell_g^+ \approx 13$ for both blade ⊓⊓ and 30° trapezoidal ⩚ riblets, especially from the shift in wavelength of the peak pressure in figure 3(*b*). However, marginal rollers are predicted in the linear-stability analysis past $\ell_g^+ \approx 14$ and $\ell_g^+ \approx 17$, respectively, for these riblet shapes. Only for 30° triangular ⩛⩛ riblets are rollers predicted at $\ell_g^+ \approx 11$, consistent with when rollers are expected from DNS (figure 3).

While the linear-stability predictions in figure 4 (solid lines) overall agree with DNS observations, the stability results themselves still implicitly depend on the DNS through the DNS-interpolated model for the eddy viscosity origin, $\ell_T^+$ (discussed in Appendix C). Thus, additional linear-stability predictions are provided in figure 4 based on *a priori* $\ell_T^+$ values (dashed lines). The *a priori* $\ell_T^+$ values are taken from the viscous vortex model of Wong *et al.* (2024) and are accurate only up to $\ell_g^+ \approx 10$, with the error in the extrapolation for larger $\ell_g^+$ shown in Appendix C. The now completely *a priori* 2-D linear-stability predictions (dashed lines) overall remain consistent with the DNS observations of spanwise rollers over riblets. The *a priori* predictions correctly identify which riblets promote rollers and which do not, and successfully sort riblet geometries by roller intensity. However, the *a priori* predictions do tend to somewhat overpredict growth rates, as the shear layer is up to $\approx 4$ viscous units thicker with the extrapolated *a priori* $\ell_T^+$ values than with the DNS-interpolated $\ell_T^+$ values. There is also some degree of sensitivity in the roller wave speed, and sometimes also roller wavelength, with small changes in $\ell_T^+$ (1–2 viscous units). Overall, further work is required to improve predictions of $\ell_T^+$ for larger riblets. Nevertheless, these results demonstrate that useful *a priori* linear-stability predictions can still be made for other riblet geometries (without further model improvements), for riblets up to and slightly past their design point of maximum drag reduction ($\ell_g^+ \approx 10$), and without running any DNS. This does not alter the main message though, i.e. that an accounting of the shift in turbulence $\ell_T^+$ is necessary to correctly predict the occurrence of rollers (figure 4*d*, comparing solid and dotted lines). Notably, taking $\ell_T^+ = 0$ (crest-origin) regardless of riblet size and shape would result in all riblet shapes tested promoting spanwise rollers for all $\ell_g^+$ past the onset of the instability (not shown). In reality, for large riblets, the turbulent flow descends into the riblet grooves (i.e. $\ell_T^+ > 0$), leading to an increased lack of mean shear and causing the rollers to decay at larger $\ell_g^+$.

The results in figure 4(*a*) also provide a means to predict the intensity of rollers over these and similarly shaped riblets. For example, weak rollers were suggested by flow-reversal within the grooves of $\ell_g^+ \approx 19$, $\alpha \approx 53°$ tip-angle triangular △△△ riblets, from the DNS of Chu & Karniadakis (1993, figure 30). Equally, weak rollers would be predicted in the linear-stability analysis, as the similarly sized $\alpha \approx 60°$ tip-angle triangular △△△ riblets have near-marginal rollers according to figure 4(*a*), and as more slender riblets tend to increase the likelihood of rollers (comparing green through purple through yellow curves, in order of decreasing $\alpha$, or increasing slenderness).

Furthermore, the 2-D linear-stability analysis also predicts that not all riblets promote rollers, unlike the 1-D analysis of García-Mayoral & Jiménez (2011*b*). Figure 4(*a*) shows that rollers would almost never form for 90° triangular △△ and asymmetric triangular ◺◺ riblets, in agreement with the lack of rollers observed for those riblet shapes in figures 1–3, and in agreement with DNS (Endrikat *et al.* 2021*a*,*b*). Note that the maximum

growth rate for a given riblet size is plotted only in figure 4(*a*) when a local maximum in growth rate is present, such that results are not plotted past $\ell_g^+ \approx 24$ for 90° triangular riblets.

These 2-D linear-stability results further demonstrate that spanwise rollers are not a maximally growing instability, as the growth rates remain near-zero (marginal) in figure 4(*a*) for riblets with sizes $10 \lesssim \ell_g^+ \lesssim 20$. Note that the growth rates from the 2-D linear-stability analysis are $\mathrm{Im}(\omega^+) \lesssim 0.04$, across a relatively wide range of $\ell_g^+$, and that these growth rates are significantly smaller than those measured for maximally growing rollers, $\mathrm{Im}(\omega^+) \approx 0.2$ (García-Mayoral & Jiménez 2011*b*). That rollers are marginal modes thereby explains the agreement between the current linear-stability predictions and those of the resolvent analysis of blade riblets in Chavarin & Luhar (2020); additional comparisons between linear-stability and resolvent analysis are provided in Appendix D. Equally, that rollers are marginal explains why García-Mayoral & Jiménez (2011*b*), who assumed maximally growing rollers, underpredicted wavelengths of $\lambda_x^+ \approx 60$ for spanwise rollers. As shown in figure 4(*b*), marginal rollers have wavelengths $100 \lesssim \lambda_x^+ \lesssim 200$, consistent with DNS. This realisation further motivates the reconsideration of a 1-D linear-stability model in § 5.

The 2-D linear-stability analysis also suggests rollers weaken and eventually vanish for all riblet shapes at larger $\ell_g^+$ (only computed up to $\ell_g^+ \approx 30$ in the linear analysis). However, some discrepancies between the linear-stability analysis and the DNS are again observed. For example, the 2-D analysis predicts that rollers would decay by $\ell_g^+ \approx 25$ for 30° trapezoidal riblets, whereas from the DNS analysis, weak rollers appear to persist until $\ell_g^+ \approx 40$, with $\max(\langle p'p' \rangle^+)/\max(\langle p'_{sm} p'_{sm} \rangle^+)$ remaining slightly above unity in figure 3(*a*), although slowly decreasing with increasing $\ell_g^+$. As an essentially inviscid instability (Jiménez *et al.* 2001; Drazin & Reid 2004; García-Mayoral & Jiménez 2011*b*), the roller mode is very sensitive to the magnitude of $\partial_{zz}U$ near the crests, which sets the size and intensity of the shear layer. With increasing riblet size, turbulence descends further within the riblet grooves, so $\ell_T^+$ increases and $\partial_{zz}U$ reduces. Perturbation energy production via $\mathrm{i}\kappa_x^+ \hat{w}^+ \partial_{zz} U^+$ thereby falls with increasing $\ell_g^+$, and so, based on the 2-D linear model with $\ell_T^+$-shifted Cess, it is only $\ell_g^+ \lesssim 30$ riblets that sustain marginal rollers. Thus, the weakening of the roller mode can be explained within the simplified framework of the linear-stability analysis. Note that rollers weaken at larger $\ell_g^+$ in spite of the increases to the wall admittance with riblet size, recalling that $\hat{w}^+/\hat{p}^+$ scales approximately linearly with $\ell_g^+$ (Endrikat *et al.* 2021*a*, figure 13*b*). In addition, the validity of the linear analysis (and this explanation) is supported by its predictions remaining generally consistent with both DNS (Endrikat *et al.* 2021*a*) at the same $Re_\tau$ and recent experiments (Abu Rowin *et al.* 2025) at much higher $Re_\tau$. Note that there is no immediate reason why the model predictions (and explanation) should be invalidated at higher $Re_\tau$, given the insensitivity of the near-wall mean-velocity curvature to $Re_\tau$, as discussed in García-Mayoral & Jiménez (2012).

Linear predictions are not provided in figure 4 for $\ell_g^+ > 30$, as the Cess approximation of the mean flow is an increasingly poor representation of the DNS mean flows for increasingly large riblets, and as the roller dynamics may become increasingly nonlinear. However, riblets are typically manufactured to ensure $\ell_g^+ \approx 10$ at their design point, as assumed in, for example, Mele *et al.* (2020) and Mele, Saetta & Tognaccini (2023), such that the eventual breakdown of the Cess approximation at larger $\ell_g^+$ barely impacts the usefulness of the 2-D predictions for riblet design.

Further improvements to the mean-flow approximation are not considered here, although the importance of various modelling choices is briefly considered for not-too-large riblets

($\ell_g^+ \approx 15$) in figure 4(*d*). As shown, the constants employed in the Cess eddy-viscosity profile, the inclusion of eddy viscosity when solving for the perturbations, and the numerical resolution, all do not greatly alter the growth rates predicted for the roller instability. The only modelling choice which proves relevant is the choice of turbulence origin $\ell_T^+$. Slight differences in the location of the turbulence origin (DNS-fitted or DNS-matched) provide commensurately small differences in the predicted growth rate, and so do not compromise growth predictions. Note that the $\ell_T^+$ values here are based on quadratic fits to DNS data and remain within $\approx \pm 30\,\%$ of DNS-matched values of $\ell_T^+$, where the DNS-matched values satisfy $\Delta U^+ = -(\ell_U^+ - \ell_T^+)$ at each DNS data point (discussed further in Appendix C). Further evidence that the fitted $\ell_T^+$ values are satisfactory is provided in Appendix E, figures 15 and 16. Predictions from riblet-resolved 2-D mean flows (with smooth-wall Cess eddy-viscosity profiles shifted by fitted-$\ell_T^+$) are shown to be consistent with predictions from DNS 2-D mean flows (Appendix E), for all riblet geometries tested. However, an unrealistic estimate for the turbulence origin, e.g. assuming the turbulence origin is at the riblet crests ($\ell_T^+ = 0$), noticeably alters the predicted growth rate, to the extent that growing or decaying rollers may be misidentified (figure 4*d*). Thus, care is warranted for very large riblets, when either selecting the virtual origin, or otherwise obtaining an estimate of the mean flow.

### 3.3. *Further evidence that the spanwise rollers are a marginal instability*

To further demonstrate that the rollers in DNS are a marginal instability, the wall admittances measured in the 2-D linear-stability analysis are compared with the wall admittances measured in DNS for Fourier modes representative of spanwise rollers ($\lambda_y^+ \to \infty$), for blade ⊓⊓ and trapezoidal ⩚⩚ riblets, up to $\ell_g^+ \approx 20$. These wall-admittance measurements are performed only to further support the finding that rollers are marginal modes, rather than as a separate means of identifying spanwise rollers, as used previously (Endrikat *et al.* 2021*a*).

The wall admittance $\hat{w}^+/\hat{p}^+$ is measured in the 2-D linear-stability analysis by superficially spanwise averaging $\hat{w}^+$ and intrinsically spanwise averaging $\hat{p}^+$ at $z^+ = -\ell_U^+$, and calculating the resulting amplitude and phase of $\hat{w}^+/\hat{p}^+$ as a function of $\lambda_x^+$. For the corresponding DNS measurements, the same process is applied for each instantaneous snapshot, of which there are $\approx 150$ to 700 snapshots depending on the case in question. From these instantaneous measurements of $\hat{w}^+/\hat{p}^+$, probability density functions of the amplitude and phase are constructed, the former with 30 logarithmically spaced bins placed between amplitudes $10^{-3}$ and 1, and the latter with 30 linearly spaced bins between $-\pi$ and $\pi$ (then translated by $2\pi$ and converted to degrees when plotted), following Endrikat *et al.* (2021*b*). To account for the logarithmically spaced bins, the probability densities for the amplitude of $\hat{w}^+/\hat{p}^+$ are premultiplied by the bin centres. Finally, note that zeroing within the roughness has not previously been observed to corrupt spectral measurements for spanwise wavelengths larger than the roughness (riblet) spacing (Sharma & García-Mayoral 2020).

As shown in figure 5, the wall-admittance amplitudes $|\hat{w}^+/\hat{p}^+|$ and phases $\angle(\hat{w}^+/\hat{p}^+)$ predicted by the 2-D linear-stability analysis are in reasonable agreement with DNS measurements, for riblets with $\ell_g^+ \gtrsim 15$ and at streamwise wavelengths $100 \lesssim \lambda_x^+ \lesssim 300$. Specifically, when growing rollers are measured in the 2-D linear-stability analysis, as indicated by the cyan portions of the solid lines in figure 5, the wall-admittance amplitudes $|\hat{w}^+/\hat{p}^+|$ and phases $\angle(\hat{w}^+/\hat{p}^+)$ are near the medians of the DNS probability density functions (ridges of the coloured contours). Thus, the spanwise rollers in the DNS resemble near-marginal modes for these blade ⊓⊓ and 30° trapezoidal ⩚⩚ riblets

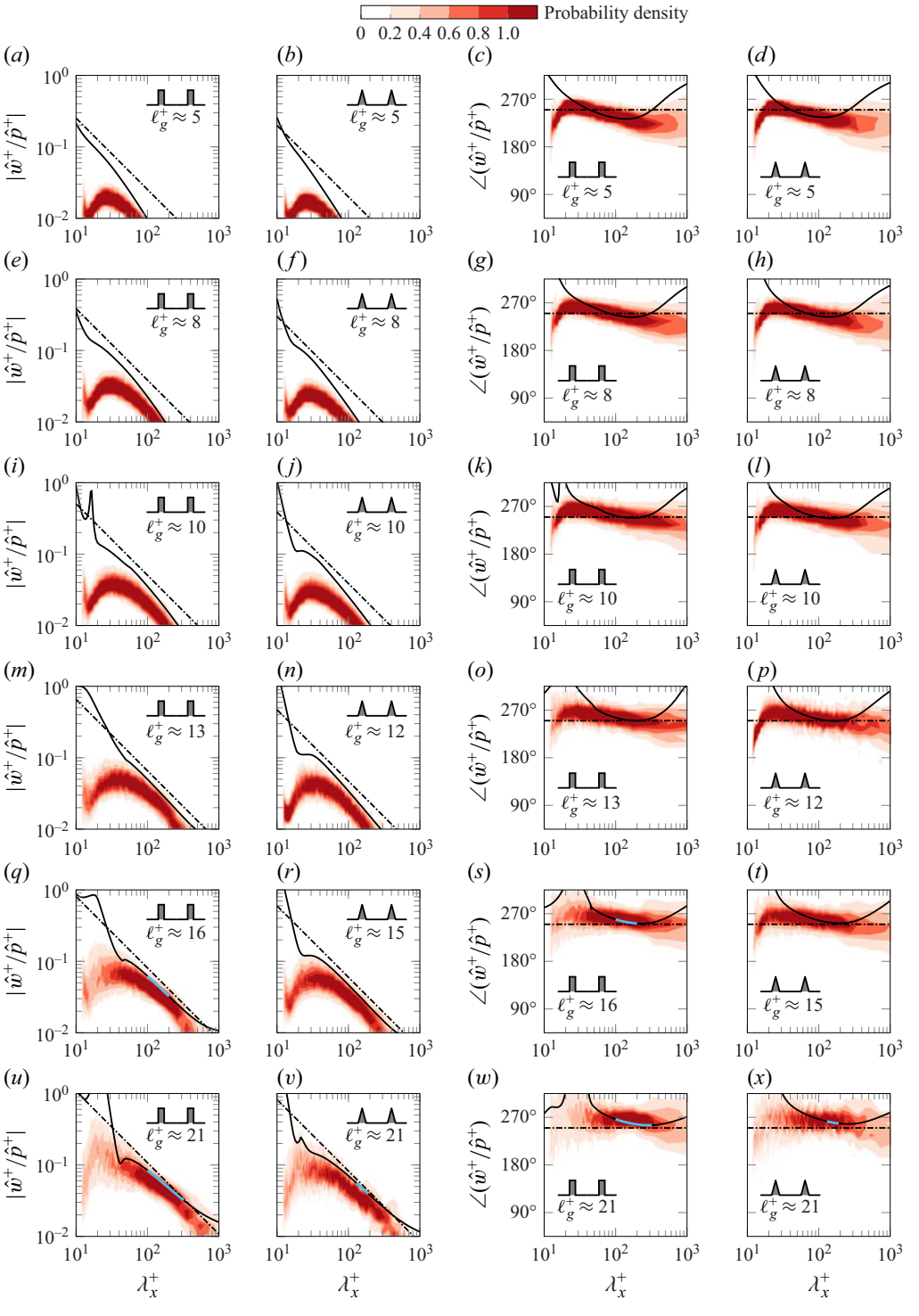


Figure 5. Comparing the wall admittance measured in the DNS with that predicted by the 2-D linear-stability analysis (measured at $z^+ = -\ell_U^+$, zeroing $\hat{w}^+$ and $\hat{p}^+$ within the riblets). Coloured contours are probability density functions from the DNS for spanwise modes with wavelengths $\lambda_y^+ \to \infty$. Solid lines are 2-D linear-stability analysis ($\kappa_y^+ = 0$ mode; black, decaying; cyan, growing). Dot-dashed black lines are from the 1-D model, (4.2).

with $\ell_g^+ \gtrsim 15$ and across $100 \lesssim \lambda_x^+ \lesssim 300$. For smaller riblets ($\ell_g^+ \lesssim 13$) and at smaller wavelengths $\lambda_x^+ \lesssim 100$, the linear-stability predictions and DNS results differ, although rollers are rarely, if ever, present in these ranges in the DNS (García-Mayoral & Jiménez 2011*b*; Endrikat *et al.* 2021*a*).

Finally, figure 5 shows that the wall-admittance amplitudes $|\hat{w}^+/\hat{p}^+|$ measured at the riblet-shape-dependent mean origin $z^+ = -\ell_U^+$ are still typically order 0.1 for roller-promoting riblets. These mean-origin admittance measurements have similar magnitudes to the crest-admittance measurements of Endrikat *et al.* (2021*a*, figure 12), and remain orders of magnitude below the wall admittances required for riblets to emulate a free-shear layer, as previously assumed (García-Mayoral & Jiménez 2011*b*). Thus, riblets appear unable to support a maximally growing Kelvin–Helmholtz mode, and at best, support its marginal precursor. However, realising that rollers are marginal is not alone sufficient for the 1-D linear-stability model of García-Mayoral & Jiménez (2011*b*) to then correctly predict rollers, or a lack thereof, for a given riblet shape. Accurate predictions for rollers also require improved approximations of both the effective wall-admittance boundary condition and the mean-velocity profile, as considered in § 4.

## 4. Towards a 1-D linear-stability model: understanding the flow dynamics within the riblet groove

Having shown that spanwise rollers can be well predicted with 2-D linear-stability analysis (§ 3), the question then becomes whether it is necessary to resolve the details of the riblet shapes, e.g. is an effective boundary condition adequate? Various approaches to obtain effective boundary conditions for riblets, or other rough or permeable surfaces, have been proposed (Luchini, Manzo & Pozzi 1991; García-Mayoral & Jiménez 2011*b*; Luchini 2013; Lācis & Bagheri 2017; Gómez-de-Segura *et al.* 2018*a*; Bottaro 2019; Bottaro & Naqvi 2020; Lācis *et al.* 2020; Naqvi & Bottaro 2021; Habibi Khorasani *et al.* 2022). These effective boundary conditions typically relate the velocity components to their gradients (or the pressure) along some plane, e.g. at the riblet crests. For example, the effective boundary conditions relevant to spanwise-infinite modes over riblets could be expressed as $\hat{u}^+ = \hat{C}_{uu}\partial_z\hat{u}^+ + \hat{C}_{up}\hat{p}^+$ and $\hat{w}^+ = \hat{C}_{wu}\partial_z\hat{u}^+ + \hat{C}_{wp}\hat{p}^+$, here expressed in Fourier space, as in Gómez-de-Segura *et al.* (2018*a*), Gómez-de-Segura & García-Mayoral (2020) and Hao & García-Mayoral (2025). The challenge is then to obtain the coefficients $\hat{C}_{uu}$, $\hat{C}_{up}$, $\hat{C}_{wu}$ and $\hat{C}_{wp}$, which in this case depend not only on the riblet size and shape, but also on $\lambda_x^+$, $\mathrm{Re}(\omega^+)$ and $\mathrm{Im}(\omega^+)$. Accurately obtaining these coefficients often relies on texture-resolved calculations in a representative volume element (Bottaro 2019), such as in the 2-D linear-stability analysis in § 3. Moreover, these coefficients provide little perspective with which to explain why only some riblets promote rollers, as it becomes difficult to inspect the relationships between the coefficients, the riblet shapes and the growth of the roller instability. However, given that the 2-D linear-stability analysis has already been performed (i.e. the $\omega^+$ of interest at which $\hat{C}_{uu}$, $\hat{C}_{up}$, $\hat{C}_{wu}$ and $\hat{C}_{wp}$ should be evaluated are already known, from § 3), an assessment of the accuracy of effective boundary conditions can be quickly made, as shown in figure 6. Even with perfect information (i.e. taking from the riblet-resolved 2-D-analysis measurements of the spanwise-averaged mean flow and spanwise-averaged perturbations) the use of a 1-D effective boundary condition placed at the riblet crests $z^+ = 0$ yields predictions with some error (comparing square markers to solid line). This error almost entirely vanishes once the 1-D effective boundary condition is placed $\approx 6$ viscous units above the riblet crests (circle markers), indicating that both spanwise variations in the mean flow and spanwise variations in the perturbations, which

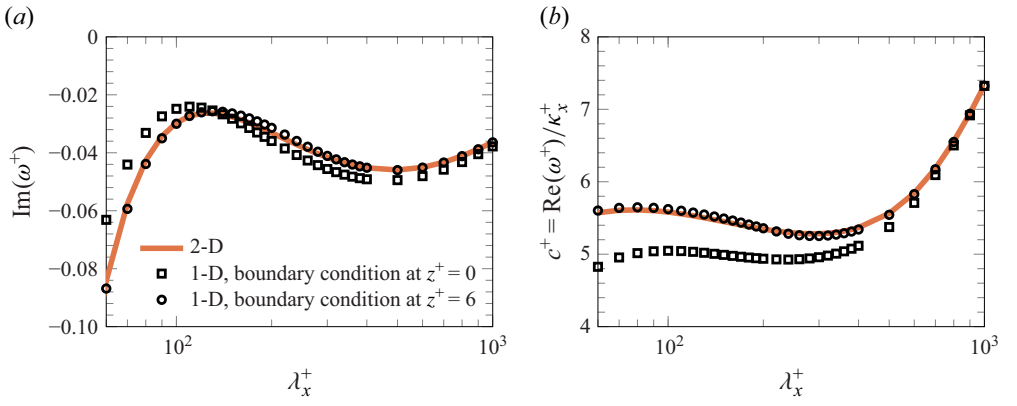


Figure 6. Testing effective boundary conditions for riblets, here, for $\ell_g^+ \approx 12$ trapezoidal riblets. (*a*) Growth rates. (*b*) Wave speeds. Solid lines are from the 2-D linear-stability analysis, identical to figures 8(*g*) and 8(*j*), respectively. Symbols are from 1-D linear-stability analysis, with more general wall-admittance boundary conditions of $\hat{u}^+ = \hat{C}_{uu}\partial_z\hat{u}^+ + \hat{C}_{up}\hat{p}^+$ and $\hat{w}^+ = \hat{C}_{wu}\partial_z\hat{u}^+ + \hat{C}_{wp}\hat{p}^+$, where $\hat{C}_{uu}$, $\hat{C}_{up}$, $\hat{C}_{wu}$ and $\hat{C}_{wp}$ were calculated for each $\lambda_x^+$ based on the growth rates and wave speeds of the leading eigenvalues from the 2-D analysis.

lead to cross-terms upon spanwise averaging, are relevant near the riblet crests ($z^+ \lesssim 6$). These spanwise variations in the riblet-resolved analysis must be captured, at least in an aggregate sense, for the 1-D analysis to be able to replicate the 2-D results. The importance of spanwise variations in the mean is further considered in § 4.2.

As calculating the coefficients $\hat{C}_{uu}$, $\hat{C}_{up}$, $\hat{C}_{wu}$ and $\hat{C}_{wp}$ for an effective boundary condition is no more informative than 2-D linear-stability analysis, the choice is instead made to develop a model boundary condition for the 1-D analysis in § 4.1. As shown in García-Mayoral & Jiménez (2011*b*), the relationship between $\hat{w}^+$ and $\hat{p}^+$ dictated the intensity of the roller instability, while Hao & García-Mayoral (2025) further highlighted the importance of the overlying pressure fluctuations in driving wall-normal transpiration. Thus, obtaining a model for the $\hat{C}_{wp}$ coefficient in particular is pursued. Furthermore, from the results presented in figure 5, such a boundary condition should relate the wall-normal velocity and pressure $\hat{w}^+/\hat{p}^+$ as a function of streamwise wavelength. For example, if $\hat{w}^+/\hat{p}^+$ varies as a decreasing function of $\lambda_x^+$, this physically represents coherent structures with large streamwise length scales struggling to penetrate the in-groove flow, and thereby experiencing a low effective wall admittance, while structures with small streamwise lengths scales experience higher wall admittances as they easily enter the riblet grooves. Such scale-dependent wall admittances have been proposed to model a range of other permeable and compliant surfaces (Brooke Benjamin 1960; Landahl 1962; Carpenter & Garrad 1986; Gómez-de-Segura *et al.* 2018*b*; Gómez-de-Segura 2019; Gómez-de-Segura & García-Mayoral 2020; Hao & García-Mayoral 2025), although scale-independent wall admittances have also been considered (Jiménez *et al.* 2001; Bottaro 2019; Motoki *et al.* 2022). Section 4.1 is thereby devoted to developing a model for the effective wall-admittance boundary condition valid for streamwise-aligned riblets, including the dependence of $\hat{w}^+/\hat{p}^+$ on the streamwise length scale $\lambda_x^+$, and on the riblet size and shape. Section 4.2 then further considers the sensitivity of marginal rollers to approximations of the mean flow, while the riblet shapes are still resolved, i.e. without simultaneously introducing uncertainty in both the approximation of the mean flow, and the effective wall-admittance boundary condition.

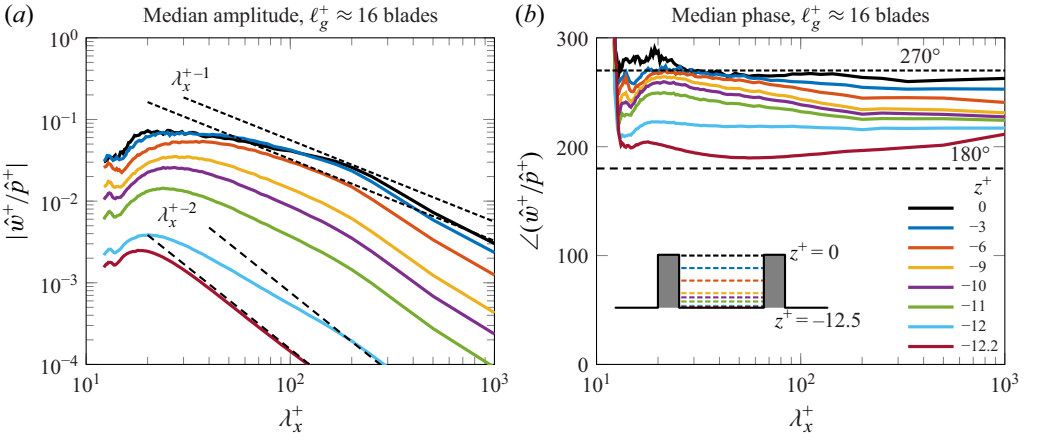


Figure 7. Median magnitude and phase of the wall admittance as a function of wall-normal height within the groove of blade riblets, to infer the dominant balances in the governing equations. An admittance magnitude varying as $\lambda_x^{+-1}$ and a 270° phase correspond to a balance dominated by unsteady inertia and overlying pressure. An admittance magnitude varying as $\lambda_x^{+-2}$ and a 180° phase correspond to a balance dominated by viscous diffusion and overlying pressure.

### 4.1. *Relating the wall admittance to the streamwise wavelength*

As a first step in developing an expression for $\hat{w}^+/\hat{p}^+$, the median amplitude and phase of the probability density functions for $\ell_g^+ \approx 16$ blade ⊓⊔⊓ riblets are plotted in figure 7 as a function of wall-normal height within the riblet groove. Note that the median amplitude (or phase) tracks the crest of the corresponding probability density function for a given wall-normal height, and that the probability density functions at $z^+ = -\ell_U^+ \approx -2.9$ were depicted in figure 5(*q*) for the amplitude, and figure 5(*s*) for the phase, for these $\ell_g^+ \approx 16$ blade ⊓⊔⊓ riblets. Figure 7 then serves to test the previous assumption that rollers experienced an effective wall admittance due to streamwise variations in the mass flux within the riblet grooves, driven by the overlying pressure and balanced by viscous diffusion (García-Mayoral & Jiménez 2011*b*). In relation to figure 7, these assumptions imply the admittance amplitude $|\hat{w}^+/\hat{p}^+|$ should vary as $\lambda_x^{+-2}$ and the admittance phase be constant at $\angle(\hat{w}^+/\hat{p}^+) = 180°$. To see this, note that the streamwise momentum equation with a dominant balance between pressure and viscous diffusion simplifies to $\nabla_{yz}^2\hat{u}^+ = \mathrm{i}\kappa_x^+\hat{p}^+$ within the groove. The in-groove velocity can be expressed as $\hat{u}^+ = -\mathrm{i}\kappa_x^+\hat{p}^+ f^+(y^+, z^+)$, as shown in García-Mayoral & Jiménez (2011*b*), by assuming the pressure is uniform within the groove cross-section and by defining an auxiliary function $f^+$ which satisfies $\nabla_{yz}^2 f^+ = -1$ (and has the same boundary conditions as $\hat{u}^+$). Substituting continuity $-\mathrm{i}\kappa_x^+\hat{u}^+ = \partial_z\hat{w}^+$ into the in-groove velocity expression, to relate $\partial_z\hat{w}^+$ to $\hat{p}^+$, yields $\partial_z\hat{w}^+ = -\kappa_x^{+2}\hat{p}^+ f^+(y^+, z^+)$. Finally, integrating across the groove cross-section (from $z^+ \leqslant 0$ to the valley) gives $\langle\hat{w}^+\rangle|_{z^+} = -(\kappa_x^{+2}\,\hat{p}^+|_{z^+}/s^+)\iint_{A_{g,z}^+} f^+\,\mathrm{d}y^+\mathrm{d}z^+$, i.e. equation (6.9) of García-Mayoral & Jiménez (2011*b*), except with $A_{g,z}^+$, the groove area below the height $z^+$, in the place of $A_g^+$, the groove area below the crests (at $z^+ = 0$) and assuming no-slip, impermeable riblet walls. The integral $\iint_{A_{g,z}^+} f^+\,\mathrm{d}y^+\mathrm{d}z^+$ is real, and depends just on the riblet geometry (García-Mayoral & Jiménez 2011*b*), so the real prefactor $\kappa_x^{+2}/s^+ = 4\pi^2/(\lambda_x^{+2}s^+)$ dictates

the scale-by-scale relationship between $\langle\hat{w}^+\rangle$ and $\hat{p}^+$ which for this pressure–viscous balance is proportional to $\lambda_x^{+-2}$ with a 180° phase difference.

As shown in figure 7, however, such a pressure–viscous-diffusion balance is only satisfied deep within the riblet grooves, within half a viscous unit of the groove floor ($z^+ \lesssim -12.2$, maroon curve, with the groove floor at $z^+ \approx -12.5$), and implying a very thin viscous sublayer for these long spanwise-wavelength $\lambda_y^+ \to \infty$ modes. Thus, beyond one viscous unit from the valley floor, the DNS measured amplitudes and phases no longer satisfy the viscous-dominated wall-admittance boundary condition assumed by García-Mayoral & Jiménez (2011*b*) for these $\ell_g^+ \approx 16$ riblets. Although much smaller riblets $\ell_g^+ \lesssim 10$ may have viscous-dominated in-groove flow, as suggested by the slightly steeper admittance trends in figure 5, these smaller riblets are equally unlikely to ever sustain rollers. Thus, a new wall-admittance boundary condition is developed, valid for riblets of sizes $10 \lesssim \ell_g^+ \lesssim 20$.

One approach that provides wall-admittance trends consistent with those in figure 7 is to assume the overlying pressure is instead balanced by unsteady inertia within the groove. Under such a pressure–unsteady-inertia balance, the streamwise momentum equation simplifies to $-\mathrm{i}\kappa_x^+ c^+ \hat{u}^+ = -\mathrm{i}\kappa_x^+ \hat{p}^+$ within the groove, and where unsteady inertia refers specifically to $\partial_t \hat{u}^+$ in this paper. Linearised mean-flow advection terms $U^+\mathrm{i}\kappa_x^+\{\hat{u}^+, \hat{v}^+, \hat{w}^+\}$, $\hat{v}^+\partial_y U^+$ and $\hat{w}^+\partial_z U^+$ are also neglected below $z^+ = -\ell_U^+$, as the mean velocity and its gradients drop noticeably within the riblet grooves. From DNS measurements for $\ell_g^+ \lesssim 20$ riblets, the superficially averaged mean velocity at the mean origin is at least half the crest mean velocity, i.e. $\langle U^+\rangle|_{z^+=-\ell_U^+} \lesssim 0.5\langle U^+\rangle|_{z^+=0}$. Only blade ⊓⊓ riblets have noticeably higher mean velocities at the mean origin, of up to $\approx 67\,\%$ of the crest velocity. Substituting continuity $-\mathrm{i}\kappa_x^+ \hat{u}^+ = \partial_z \hat{w}^+$ into the streamwise momentum equation to eliminate $\hat{u}^+$ provides $\partial_z \hat{w}^+ = -\mathrm{i}\kappa_x^+ \hat{p}^+/c^+$. Applying the same technique as previously and integrating over the groove area yields $\langle\hat{w}^+\rangle|_{z^+} = -[\mathrm{i}\kappa_x^+ \hat{p}^+|_{z^+}/(c^+ s^+)] \iint_{A_{g,z}^+} \mathrm{d}y^+\mathrm{d}z^+$ for any $z^+ \leqslant 0$, under the same assumption of a pressure uniformly equal to $\hat{p}^+|_{z^+}$ over the groove cross-section and with impermeable riblet walls. Evaluated at the virtual origin for the mean flow, this yields a wall-admittance boundary condition of

$$\left.\frac{\langle\hat{w}^+\rangle}{\hat{p}^+}\right|_{z^+=-\ell_U^+} = \frac{-\mathrm{i}\kappa_x^+}{c^+}\frac{A_{g,-\ell_U}^+}{s^+}, \tag{4.1}$$

where $A_{g,-\ell_U}^+$ is the groove area below $z^+ = -\ell_U^+$ and where $z^+ = 0$ is at the riblet crests. Expressing the effective boundary condition as (4.1) showcases the relationship between the wall admittance and the riblet geometry, via $A_{g,-\ell_U}^+/s^+$, which may not have been readily apparent from brute-force calculations of the wall-admittance coefficient $\hat{C}_{wp}$ for different riblet sizes. The effective boundary condition (4.1) is composed of $-\mathrm{i}\kappa_x^+/c^+ = -2\pi\mathrm{i}/(\lambda_x^+ c^+)$ multiplied by the real, purely geometric factor $A_{g,-\ell_U}^+/s^+$, and further highlights that having assumed a balance between pressure and unsteady inertia within the groove provides a wall admittance proportional to $\lambda_x^{+-1}$ and a constant 270° phase difference when $c^+$ is real (i.e. the mode is marginal), consistent with the trends in DNS shown in figure 7. Specifically, the wall-admittance amplitudes measured in DNS vary as $\lambda_x^{+-1}$ at wall-normal heights near the mean origin ($z^+ = -\ell_U^+$), while the wall-admittance phases are slightly lower than 270°, but still remain reasonably constant across $\lambda_x^+$. Only much deeper within the riblet grooves, between $-12 \lesssim z^+ \lesssim -6$, are both unsteady inertia

and viscous diffusion equally relevant in balancing the overlying pressure. Similarly, the 2-D linear-stability analysis predicted trends of $\lambda_x^{+-1}$ for the admittance and $\approx 270°$ for the phase at $z^+ = -\ell_U^+$, when rollers were near marginal, recalling figure 5. Thus, in the 1-D analysis, a pressure–unsteady-inertia balance will be encoded in the effective wall-admittance boundary condition at $z^+ = -\ell_U^+$, rather than a pressure–viscous-diffusion balance.

To further reinforce that a pressure–unsteady-inertia balance is dominant near $z^+ \approx -\ell_U^+$, the model boundary condition (4.1) is compared with 2-D linear-stability analysis and DNS measurements in figure 5, taking a fixed (real) wave speed of $c^+ = 6$; see (4.2). When rollers are near marginal, the wall-admittance amplitudes given by (4.2), dot-dashed lines, agree well with the wall-admittance amplitudes measured from the 2-D linear-stability analysis, solid black/cyan lines, and from DNS, coloured contours. This agreement is observed in both the matched $\lambda_x^{+-1}$ trends with streamwise wavelength, and the approximate $A^+_{g,-\ell_U}/s^+$ scaling of the wall-admittance amplitude with riblet size. Thus, the 1-D boundary condition (4.2), which captures the importance of unsteady inertia within the riblet grooves, reasonably represents the admittance amplitude provided by grid-resolved riblets. However, the admittance phases measured in the 2-D linear-stability analysis and DNS at $z^+ = -\ell_U^+$ are slightly lower than the predicted phase of 270° from (4.1). Thus, (4.1) is henceforth approximated as

$$\left.\frac{\hat{w}^+}{\hat{p}^+}\right|_{z^+=-\ell_U^+} = \frac{\kappa_x^+}{c_{ref}^+}\frac{A^+_{g,-\ell_U}}{s^+}\exp(\mathrm{i}\phi_{ref}), \tag{4.2}$$

taking $c^+_{ref} = 6$ as a typical reference wave speed and $\phi_{ref} = 250°$ as a typical phase for near-marginal spanwise rollers, and having verified that taking $\phi_{ref} = 250°$, consistent with DNS (figure 5), yields slightly more accurate predictions than $\phi_{ref} = 270°$. Equation (4.2), in addition to a no-slip condition $\hat{u}^+ = 0$, then form the effective boundary conditions to be applied in the 1-D analysis.

### 4.2. *Approximations to the mean-velocity profile: are spanwise variations important?*

There is the potential for a greater degree of error when performing 1-D rather than 2-D analysis, as both the effective boundary condition and mean-velocity profile are approximated. As was shown in figure 6, however, these errors vanish when both (i) rigorous boundary conditions relating both $\hat{u}^+$ and $\hat{w}^+$ to both $\partial_z\hat{u}^+$ and $\hat{p}^+$ are obtained (instead of modelling these relationships) and (ii) the effective boundary conditions are placed above the riblet crests, in a region where the mean flow is spanwise uniform (and using this spanwise-uniform mean flow in the 1-D analysis). Error (ii) specifically stems from the absence of cross-terms in the 1-D analysis. Cross-terms of the form, for example, $\langle(U^+ - \langle U^+\rangle_y)\mathrm{i}\kappa_x^+(\hat{u}^+ - \langle\hat{u}^+\rangle_y)\rangle_y$, result from taking the 2-D advection term $U^+(y^+, z^+)\mathrm{i}\kappa_x^+\hat{u}^+(y^+, z^+)$, subtracting the 1-D advection term $\langle U^+\rangle_y\mathrm{i}\kappa_x^+\langle\hat{u}^+\rangle_y$, and spanwise averaging. Note that cross-terms also immediately vanish if the 2-D mean flow happens to be spanwise uniform, such that error (ii) is non-zero only below a certain wall-normal height.

The importance of the cross-terms, and thereby the spanwise variations in the mean, are here considered by modifying the mean flow, while applying impermeable, no-slip boundary conditions on the perturbations along the riblet surface. This avoids simultaneously introducing uncertainties in the modelling approximations for both the mean flow and the perturbations. Specifically, the cross-terms are eliminated from the 2-D analysis (figure 8) by replacing the spanwise-varying mean flow $U^+(y^+, z^+)$ with

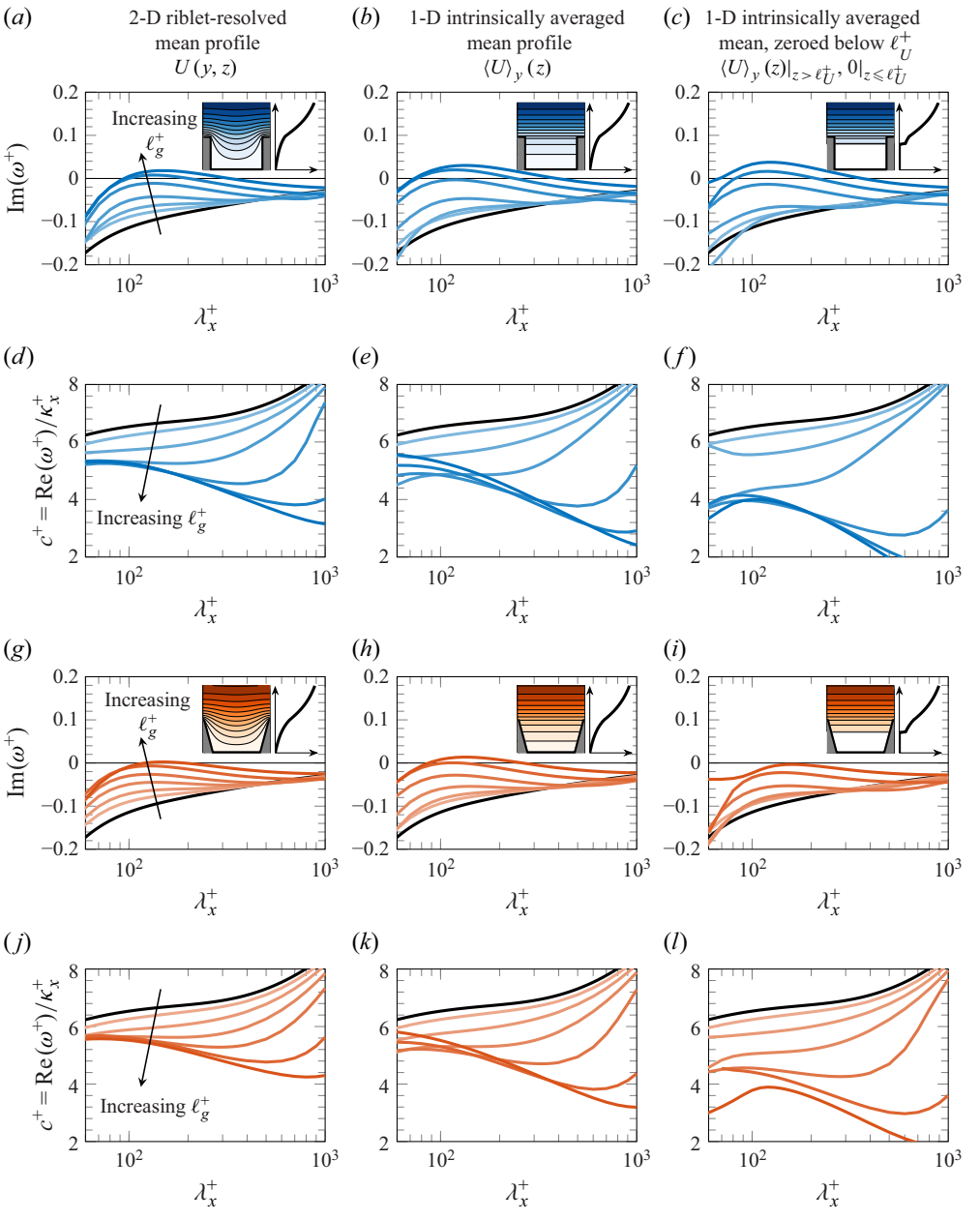


Figure 8. Assessing the importance of spanwise variations in the mean flow. Growth rates and wave speeds predicted for rollers over blade and trapezoidal riblets obtained with spanwise-uniform mean flows (middle column), remain similar to those with spanwise-varying mean flows (left column; as in figure 4). Zeroing the mean flow below the mean origin $z^+ = -\ell_U^+$ (right column) is also relatively unimportant when it comes to predicting the roller growth rates, but tends to underpredict wave speeds. Note that the superficial averages of the mean flows above $z^+ = -\ell_U^+$ (right column) are identical to those used in the 1-D linear-stability analysis (figure 9).

its spanwise average $\langle U^+\rangle_y(z^+)$. Here, the intrinsic average is used below the crests (as defined in Appendix E), to ensure a smooth wall-normal variation in the 1-D superficially averaged mean-velocity profile even if there is a sudden change in the fluid volume fraction, e.g. as for blade riblets. As shown in figure 8, the growth-rate and wave-speed predictions based on both spanwise-varying mean flows (left column, with cross-terms), and intrinsically averaged spanwise-uniform mean flows (middle column, without cross-terms) are similar, for the riblets of sizes $\ell_g^+ \lesssim 20$ tested. Thus, it is unlikely that the cross-terms, that are by default absent in the 1-D analysis, will greatly impact the accuracy of the 1-D predictions, based on this 2-D analysis with and without cross-terms. Equally, spanwise variations in the mean flow are a detail which need not be retained in the 1-D analysis, in any sense, to predict rollers reasonably well for riblets of sizes $\ell_g^+ \lesssim 20$.

The importance of the mean profile below the mean-flow origin $\ell_U^+$ is then considered. Although capturing the full extent of the shear layer (up to $z^+ = -\ell_U^+$) is important when predicting rollers (Sharma & García-Mayoral 2020), the details of the mean flow below $z^+ = -\ell_U^+$ may not be relevant. As shown in figure 8, zeroing the mean velocity below $z^+ = -\ell_U^+$ yields growth-rate predictions (right column) which remain similar to those with unmodified mean flows (left column). However, zeroing below $z^+ = -\ell_U^+$ reduces the wave speeds predicted for larger riblets, indicating that rollers are sensitive to the mean-velocity profile within the riblet grooves. Although not shown here, linearly extrapolating the spanwise-averaged velocity profile below the crests of the riblets, such that $\langle U^+\rangle_e(z^+) = 0$ at $z^+ = -\ell_U^+$, also led to an underprediction of wave speeds. Thus, although spanwise variations in the mean profile are unimportant to the growth of the spanwise roller instability (for $\ell_g^+ \lesssim 20$), the wave speed can be inaccurately predicted when the in-groove mean flow is not well approximated, e.g. by zeroing the mean velocity at or below $z^+ = -\ell_U^+$.

Based on the similarities in the growth rates shown in figure 8, the superficial averages of the riblet-resolved 2-D mean profiles will be employed in the 1-D linear-stability analysis in § 5. The 1-D analysis then requires a single riblet-resolved 2-D calculation per riblet size, with an $\ell_T^+$-shifted smooth-wall Cess eddy-viscosity profile, to obtain the superficially averaged mean flow. Note that the growth rates predicted from 1-D mean flows, calculated with a boundary condition of $U^+ = 0$ at $z^+ = -\ell_U^+$, and still with $\ell_T^+$-shifted Cess profiles, were not consistent with predictions from 2-D calculations, as shown in Appendix E, figure 15. However, to demonstrate that the 1-D analysis can still provide useful standalone predictions, i.e. without any assisting 2-D calculations, results from 1-D linear-stability analysis with 1-D mean flows ($U^+ = 0$ at $z^+ = -\ell_U^+$) are also included.

## 5. The 1-D linear predictions based on a dynamical model of the in-groove flow

As posed at the start of § 4, the question of whether the riblets can be adequately replaced by an effective boundary condition is now considered. This involves the use of the model boundary condition (4.2), as a means to relate the riblet geometry to the wall admittance, and thereby explain why only some riblets promote spanwise rollers.

The 1-D analysis is performed in MATLAB, solving a primitive variable formulation of the linearised Navier–Stokes equations, based on Luhar, Sharma & McKeon (2014) and Luhar, Sharma & McKeon (2015). The no-slip ($\hat{u}^+ = \hat{v}^+ = 0$) and wall-admittance (4.2) boundary conditions are placed at $z^+ = -\ell_U^+$, and implemented with row replacement. Symmetry conditions at the centreline follow from appropriate modifications to the spectral differentiation matrices (Weideman & Reddy 2001), with interest in symmetric streamwise velocity perturbations. The lower half of the domain is then discretised with

$N_c = 160$ Chebyshev nodes (for $Re_\tau = 395$), in line with the $N_c \geqslant 100$ Chebyshev nodes (half-domain) of Luhar *et al.* (2015), and the $N_s = 200$ splines (full domain) of Jiménez *et al.* (2001), both at $Re_\tau \approx 2003$. The eigenvalue problem is solved in generalised form using the function eigs with tolerance $10^{-12}$, and targeting the leading four eigenvalues near $c^+ \approx 6$. Eigenvalues which prove sensitive to grid resolution with tolerance $10^{-3}$ (comparing $N_c = 160$ to $N_c = 170$) are omitted, although spurious modes are typically far from the eigenmode of interest.

### 5.1. *Predictions of the 1-D linear-stability analysis*

The results of the 1-D and 2-D analyses are compared in figure 9. Overall, the 1-D analyses (figure 9, middle and right columns) provide predictions which are reasonably consistent with those of both the 2-D linear-stability analysis (figure 9, left column) and the DNS, in terms of which riblet shapes promote rollers. Specifically, both 1-D analyses predict that 30° triangular riblets should form rollers at the smallest $\ell_g^+$ values and should promote the most intense rollers, followed then by blade, 60° triangular and 30° trapezoidal riblets, respectively. This ordering of roller intensities is similar to that observed in both the 2-D linear-stability analysis and DNS, and follows from the scaling of the wall-admittance boundary condition (4.2) with riblet size and shape, and streamwise scale. The $\lambda_x^{+-1}$ variation with streamwise scale penalises the wall admittance less aggressively at larger streamwise wavelengths (than a $\lambda_x^{+-2}$ scale dependence), in line with a balance between unsteady inertia and pressure within the riblet grooves. This allows for larger wall admittances at the streamwise wavelengths $90 \lesssim \lambda_x^+ \lesssim 140$, figure 9(*d*), at which rollers are predicted in the 1-D analysis. Equally, the $A^+_{g,-\ell_U}/s^+$ scaling of the wall-admittance boundary condition (4.2) captures enough of a measure of the riblet size and shape, particularly the riblet slenderness (per $\ell_g$), i.e. $A_{g,-\ell_U}/(\ell_g s)$, so as to provide reasonable predictions in the 1-D analysis (further evidence is provided in Appendix F by comparing the leading eigenmodes from the 2-D and 1-D analyses). The riblet slenderness $A_{g,-\ell_U}/(\ell_g s)$ is expressed per $\ell_g$ to enable comparison at roller-onset sizes of matched $\ell_g^+ \approx 10$ (García-Mayoral & Jiménez 2011*b*), and so provides a rough guide as to which riblet shapes are likely to have the most intense rollers. These slenderness values $A_{g,-\ell_U}/(\ell_g s)$ are, , 0.77; , 0.49; , 0.42; , 0.38; , 0.28; , 0.26. Thus, the ordering of roller intensity from the 2-D linear-stability analysis and DNS is (approximately) reproduced, just from this $A_{g,-\ell_U}/(\ell_g s)$ measure of riblet slenderness, as informed by the development and modelling of the wall-admittance boundary condition in § 4.1.

## 6. Conclusions

This paper has highlighted the importance of riblet-resolved calculations for accurately predicting spanwise roller instabilities forming over riblets, and more generally, of the importance of texture-resolved calculations to inform modelling choices for non-smooth surfaces. Riblet-resolved calculations proved important both in establishing when and why effective boundary conditions break down, and in identifying the key features of the mean flow within the riblet grooves. Furthermore, physical insights into the flow dynamics in a linearised setting proved consistent with new insights from DNS analysis, and reasonable predictions for which riblet sizes and shapes promote rollers were obtained with both the *a priori* and *a posteriori* 2-D models.

Through the use of riblet-resolved 2-D linear-stability analysis, in concert with DNS and 1-D linear-stability analysis, previous theories regarding spanwise rollers

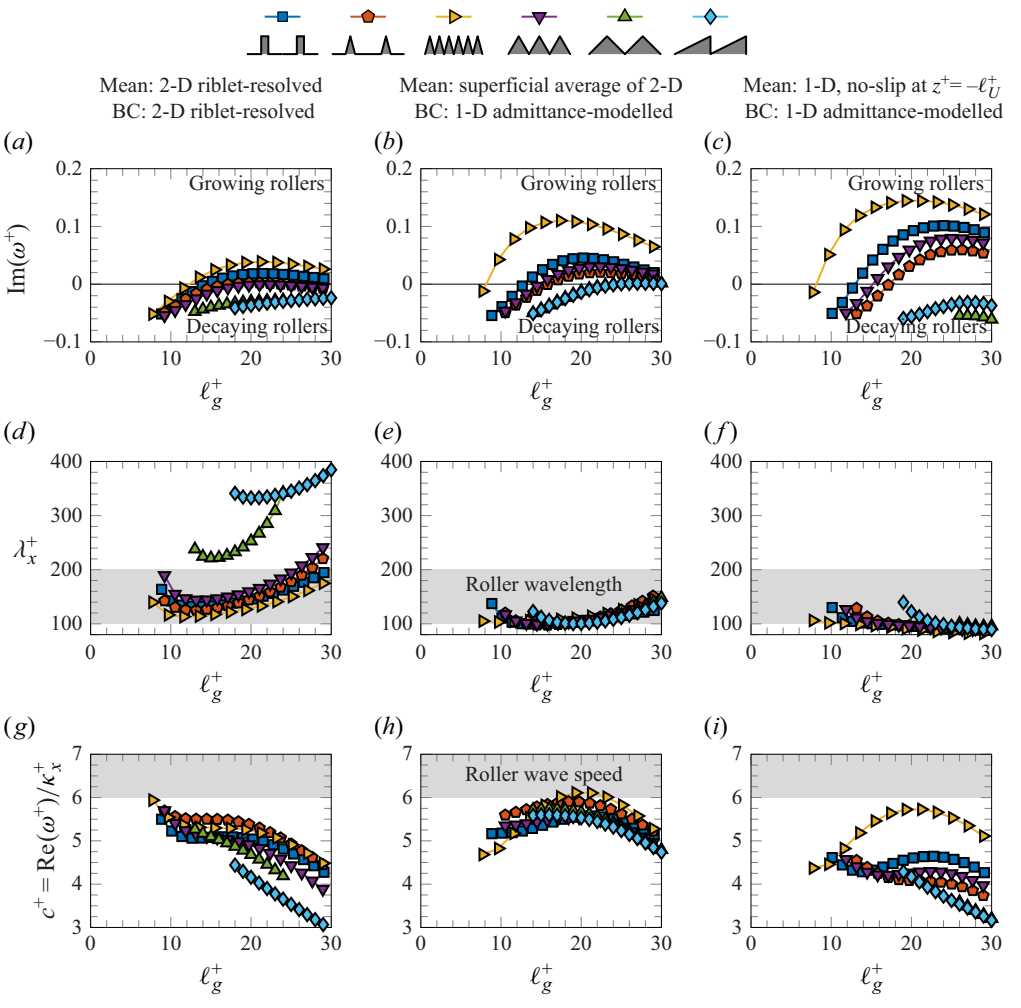


Figure 9. Comparing the 2-D linear-stability analysis which resolves the riblets (left column) to the 1-D analysis with a wall-admittance model capturing the in-groove physics (middle and right columns). The 1-D wall-admittance boundary conditions are $\hat{w}^+/\hat{p}^+ = (A^+_{g,-\ell_U}/s^+)(\kappa_x^+/6)\exp(250\pi\mathrm{i}/180)$ and $\hat{u}^+ = 0$ at $z^+ = -\ell_U^+$. The 1-D analysis is performed both with superficially averaged mean-velocity profiles obtained from riblet-resolved 2-D calculations for each riblet size (middle column) and with mean-velocity profiles obtained over no-slip walls placed at $z^+ = -\ell_U^+$ (right column), so as to provide a set of standalone 1-D predictions. Overall, the 1-D analysis reasonably captures the prevalence or lack of rollers based on the roller growth rates (first row), as well as the roller wavelengths (second row) and wave speeds (third row). However, the 1-D analysis tends to predict growing rollers at smaller $\ell_g^+$ than the 2-D analysis, and tends to underpredict the wave speeds when using 1-D mean flows over a no-slip wall (right column), as the 2-D superficially averaged mean flows retain a slip velocity at $\ell_U^+$.

(García-Mayoral & Jiménez 2011*b*) were reappraised. First, riblet grooves did not provide sufficient wall admittance to emulate a free-shear layer. Thus, maximally growing free-shear-layer instabilities are not promoted by riblets, with the rollers over riblets therefore not strictly Kelvin–Helmholtz rollers. The rollers are sensitive to (i) the finite wall admittance of the riblets, (ii) the mean shear in the mixing layer (which depends critically on the choice of turbulence origin $\ell_T^+$) and (iii) the details of the mean-velocity profile

within the riblet grooves, the latter two related to the momentum absorption near the riblet tips (Endrikat *et al.* 2021*a*).

The spanwise rollers, being far from the maximally growing limit, were further shown to be near-marginally-stable modes. This finding suggests that the spanwise rollers forming over some other non-smooth surfaces may also be marginal modes, especially whenever rollers form with similar streamwise wavelengths $\lambda_x^+ \approx 150$ to those over riblets, e.g. as observed for some permeable substrates (Gómez-de-Segura & García-Mayoral 2019; Chavarin *et al.* 2021). The characteristics of the marginal rollers over riblets, as predicted by the 2-D linear-stability analysis herein, also matched DNS observations (García-Mayoral & Jiménez 2011*b*, 2012; Endrikat *et al.* 2021*a*) and 2-D resolvent predictions (Chavarin & Luhar 2020), having streamwise wavelengths of $\lambda_x^+ \approx 150$ and wave speeds $c^+ \approx 5$. This resolved previous discrepancies in the predictions of $\lambda_x^+ \approx 60$ for the streamwise wavelength of assumed-maximally growing rollers (García-Mayoral & Jiménez 2011*b*; Gómez-de-Segura *et al.* 2018*b*), compared with the wavelength $\lambda_x^+ \approx 150$ of marginal rollers shown herein and in resolvent analyses (Chavarin & Luhar 2020; Chavarin *et al.* 2021). Furthermore, the 2-D linear-stability analysis correctly identified which riblet shapes promote (marginal) spanwise rollers, and which did not, in agreement with DNS observations. With a model for the turbulence origin $\ell_T^+$, this formed a predictive tool able to determine which riblets promote rollers. It still remains to determine the drag contribution attributed to the additional Reynolds stresses carried by the rollers, which has yet to be definitively measured (Endrikat *et al.* 2021*a*; Viggiano *et al.* 2024), and which ultimately requires an improved means of measuring or modelling the turbulence origin $\ell_T^+$. In addition, it remains to clarify the mechanism(s) responsible for the complete drag-reduction breakdown for all riblet shapes (Modesti *et al.* 2021; Endrikat *et al.* 2022; Chan *et al.* 2023).

With the overall success of the 2-D linear-stability analysis, the viability of accurate 1-D linear predictions was reconsidered. This required a 1-D effective boundary condition to represent the riblets, with the choice made to model the boundary condition with a wall admittance, toward identifying which geometrical features of a given riblet shape promote rollers. As shown herein, the wall-admittance measurements from both DNS and 2-D linear-stability analysis were at odds with the conventional theory of viscous-dominated in-groove physics, which informed previous 1-D modelling (García-Mayoral & Jiménez 2011*b*). Instead, for roller-promoting riblets, the overlying pressure, which drives the roller instability, was shown to be balanced by unsteady inertia within the groove. Only within half a viscous unit of the groove floor was viscous-dominated flow physics recovered. This pressure–unsteady-inertia balance revealed the importance of riblet slenderness in controlling the intensity of spanwise rollers, via the effective wall admittance. This pressure–unsteady-inertia balance also explained, for example, why rollers are promoted by slender 30° triangular riblets and not by less-slender 90° triangular riblets.

Once applied in the 1-D analysis, this wall-admittance boundary condition provided reasonable predictions as to which riblet shapes promote rollers, for riblets with grooves sizes $10 \lesssim \ell_g^+ \lesssim 20$. This 1-D boundary condition appropriately captured both the scaling of the wall admittance with riblet size and streamwise scale, which was further reflected in the 1-D analysis reasonably predicting the streamwise wavelength for maximum growth ($\lambda_x^+ \approx 100$). The 1-D analysis also indicated that intense rollers would form for the most slender riblets, 30° triangular and blade riblets especially, as in DNS. However, even though this 1-D effective boundary condition captured the in-groove physics, the 1-D analysis was unable to conclusively identify whether certain riblet shapes never promote spanwise rollers at very large riblet sizes $\ell_g^+ \gtrsim 25$. For these very large

riblets, the effective wall-admittance boundary condition broke down, with the accuracy of the mean-flow approximation a secondary (but still relevant) concern.

Beyond this, the model reduction, from DNS to 2-D to 1-D linear-stability analysis, still served to provide a generalisable and predictive explanation for rollers, i.e. a relationship between a purely geometric parameter, the riblet slenderness, $A_{g,-\ell_U}/(\ell_g s)$, and the dynamics (intensity) of the spanwise rollers. Identifying the correct physical balance within the riblet grooves directly indicated the importance of riblet slenderness, without having to rely on any correlations in DNS. Riblet slenderness being a shape-dependent quantity also explained why only some riblets (at matched size) promote rollers, as (i) groove area is only size-dependent, and (ii) marginal rollers are more sensitive to changes in the effective wall admittance than maximally growing rollers. These findings stand in stark contrast to the previous theory, which suggested that all sufficiently large riblets should form maximally growing rollers (García-Mayoral & Jiménez 2011*b*).

Given that a 1-D wall-admittance boundary condition can predict marginal spanwise rollers for riblet sizes of practical relevance, similar analyses may prove insightful for other surfaces, e.g. for high-admittance permeable substrates (Zampogna & Bottaro 2016; Lācis & Bagheri 2017; Habibi Khorasani *et al.* 2024), which, although drag increasing (Chu *et al.* 2019; Shahzad, Hickel & Modesti 2023; Hartog *et al.* 2024), may serve to mitigate noise or enhance heat transfer. This work also cautions results derived solely from modelled boundary conditions without accompanying texture-resolved calculations, e.g. for permeable substrates modelled with a scale-independent wall admittance (Jiménez *et al.* 2001; Motoki *et al.* 2022), as although linear-stability analysis may be consistent with DNS using the same modelled boundary conditions, the observed modes may not be realisable from any manufactured surface. Thus, texture-resolved calculations should be leveraged, if a parametric sweep would prove affordable, e.g. to analyse the permeable substrates directly. Otherwise, a smaller number of texture-resolved calculations should be performed and interrogated, so as to develop an effective model boundary condition able to relate the substrate properties to the dynamics of the overlying rollers.

**Acknowledgements.** D.C. is grateful for discussions with Professor L. Tuckerman who alerted him to real zero imaginary frequency (RZIF), and C.C. and D.C. are grateful for discussion with Professor P. Luchini regarding the derivation and measurement of effective boundary conditions.

**Funding.** This material is based on work supported by the Air Force Office of Scientific Research (AFOSR) under awards FA2386-23-1-4071 and FA2386-21-1-4018 (program managers: David J. Newell and Ryan W. Carr, AOARD) and on work supported by the Australian Research Council Discovery Project DP170102595. M.L. acknowledges financial support from the AFOSR under award FA9550-19-1-7027 (program managers: Douglas R. Smith and Gregg L. Abate) and the National Science Foundation under grant no. 1943105. R.G.M. acknowledges financial support from the AFOSR under award FA8655-22-1-7062. This work was partially supported by a grant from the Simons Foundation during D.C'.s visit to the Isaac Newton Institute for Mathematical Sciences, Cambridge, UK, in March–April 2022. This work was also carried out while D.C. was a visiting fellow at the Sidney Sussex College, Cambridge, UK, in May–June 2022. This research was supported by the Research Computing Services of the University of Melbourne and by the Australian Government's National Collaborative Research Infrastructure Strategy (NCRIS), with access to computational resources provided by the National Computational Infrastructure and Pawsey Supercomputing Centre through the National Computational Merit Allocation Scheme.

**Declaration of interests.** The authors report no conflict of interest.

## Appendix A. Pressure cospectra for different riblet sizes and shapes

As discussed in § 2, and recalling figure 3(*b*), the presence of spanwise rollers is indicated by a shift in the streamwise wavelength of the peak pressure from $\lambda_x^+ \approx 200$ to $\lambda_x^+ \approx 150$. This shift is relatively consistent across wall-normal heights, up to $z^+ \approx 20$, given

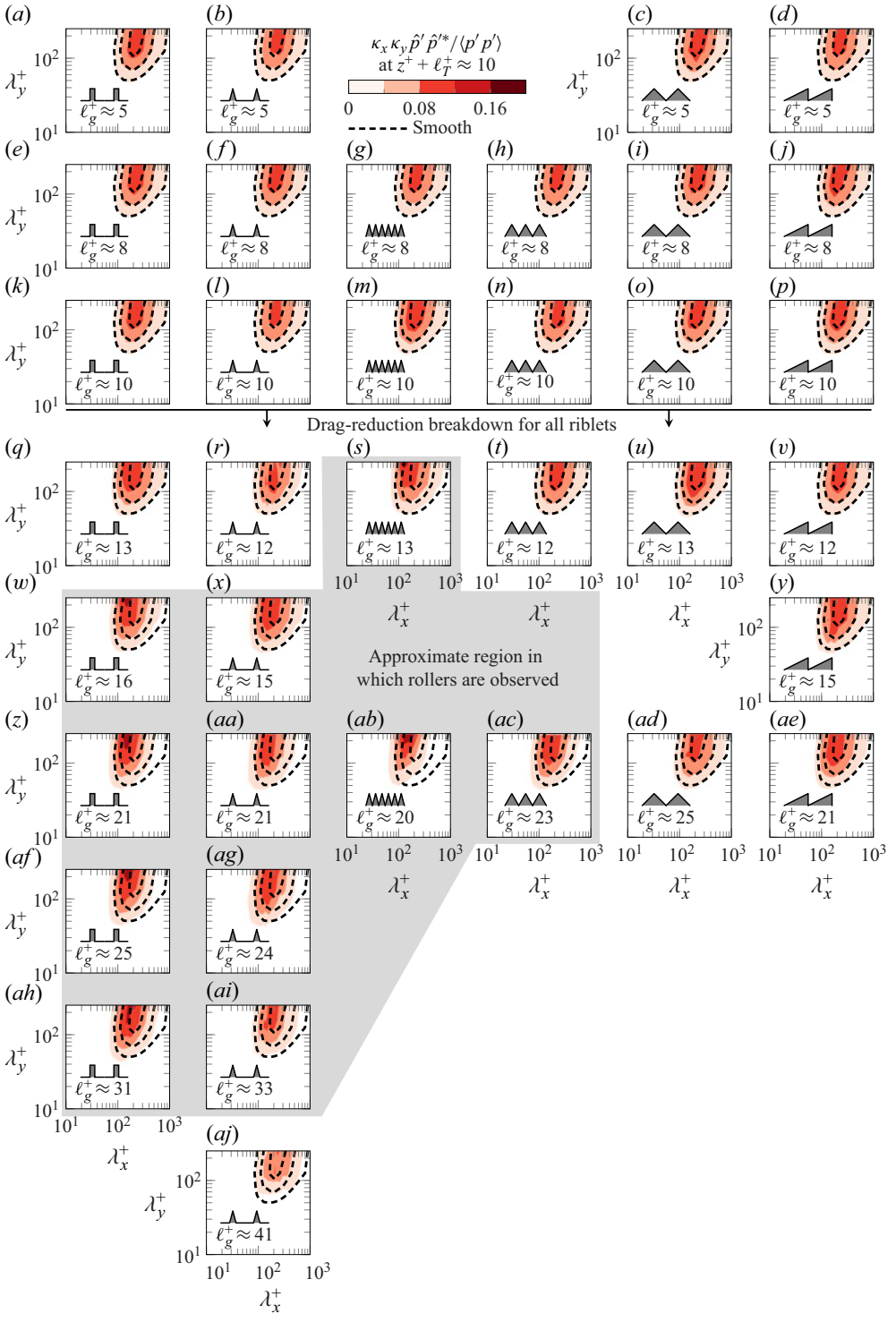


Figure 10. Cospectra of $\hat{p}'\hat{p}'^*$ normalised by the $x$-$y$-$t$ averaged $\langle p'p' \rangle$ at $z^+ + \ell_T^+ \approx 10$ for riblets of various shapes and sizes (coloured contours) and a smooth wall (black dashed lines), having reprocessed the DNS datasets of Endrikat *et al.* (2021*a*), Modesti *et al.* (2021) and Wong *et al.* (2024).

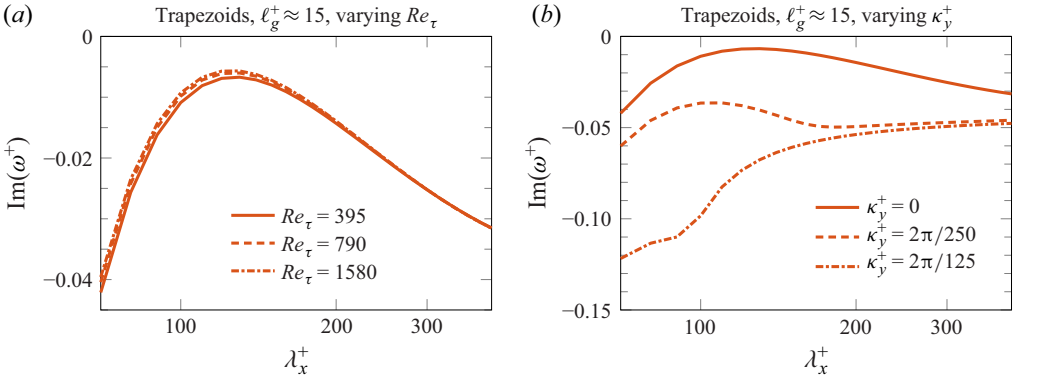


Figure 11. Growth rates for $\ell_g^+ \approx 15$ trapezoidal riblets: (*a*) varying $Re_\tau$, (*b*) varying $\kappa_y^+$. Note the different axis scales.

the uniformity of the pressure cospectra in $z^+$. As shown in figure 10 at a wall-normal height $z^+ + \ell_T^+ \approx 10$, an approximate region in which rollers are observed can be delimited solely based on this shift in the peak pressure (grey shaded region). Note that besides this shift in the pressure cospectra, the overall distribution of $\hat{p}'^+ \hat{p}'^{+*}$ across streamwise and spanwise wavelengths remains for the most part unchanged (relative to a smooth wall) by the presence of roller modes, where the superscript $()^*$ denotes the complex conjugate.

## Appendix B. Varying the friction Reynolds number and spanwise wavenumber

Taking trapezoidal riblets as a representative shape, figure 11(*a*) serves to demonstrate that the growth rates predicted in the 2-D linear-stability analysis are almost unaffected by the choice of $Re_\tau$, testing from $Re_\tau = 395$ to $Re_\tau = 1580$, and indicating that rollers are a viscous-scaled instability. This is consistent with the DNS results of García-Mayoral & Jiménez (2012), who showed that rollers over riblets scale with the distance from the wall to the local minimum in the second derivative of the mean-velocity profile (García-Mayoral & Jiménez 2011*b*), which remains constant in viscous units. This result is also recovered in the 1-D linear-stability analysis (not shown). Comparatively, rollers which form over uniform-admittance permeable substrates tend to be $\delta$-scaled (Jiménez *et al.* 2001; Motoki *et al.* 2022), not viscous-scaled, given the much larger streamwise wavelengths $\lambda_x^+ \approx 10^4$ to $10^5$ at which $\delta$-scaled rollers are marginally stable (Jiménez *et al.* 2001). Note that in this section the Cess constants themselves are kept fixed at $\kappa = 0.46$ and $A = 30.7$, while the Cess eddy-viscosity profile (Reynolds & Tiederman 1967) accounts for the varying $Re_\tau$.

In addition, figure 11(*b*) demonstrates that the spanwise-infinite mode $\kappa_y^+ = 0$ is the least stable of the large spanwise-wavelength modes ($\lambda_y^+ \gtrsim 125$), as relevant to spanwise rollers. Modes at finite $\kappa_y$ are still obtained by solving (3.1)–(3.4), except spanwise derivative terms $\partial_y$ are replaced by $(\mathrm{i}\kappa_y^+ + \partial_{\tilde{y}})$, where $\tilde{y}^+$ is $s^+$-periodic and $y^+$ is $2\pi s^+/\kappa_y^+$-periodic.

## Appendix C. Selecting the turbulence origin (for the Cess eddy-viscosity profile)

For riblets, selecting the value of $\ell_T^+$ fixes the origin of the eddy-viscosity profile $\nu_{e,S}^+(z^+ + \ell_T^+) = \nu_{e,R}^+(z^+)$. However, measuring $\ell_T^+$ from the DNS would not allow for *a priori* predictions of spanwise rollers, even assuming that $\ell_T^+$ (or a zero-plane

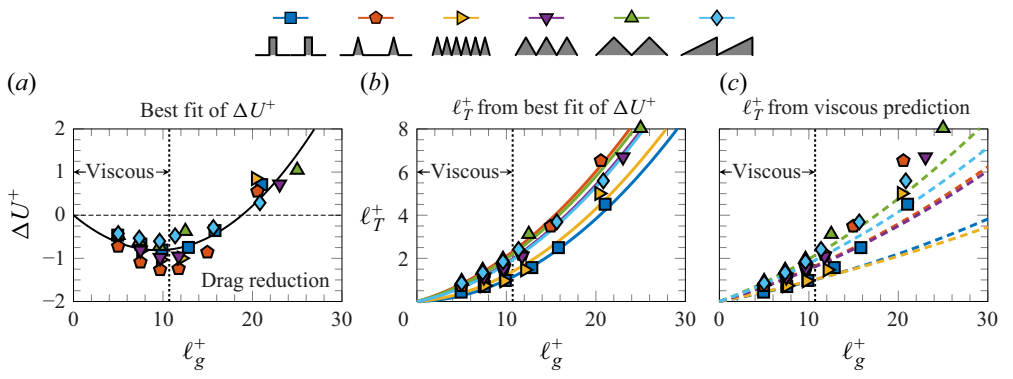


Figure 12. Selecting the turbulence origin $\ell_T^+$ to apply in the riblet-resolved linear-stability analysis, which sets the origin of the eddy-viscosity profile $\nu_{e,R}^+$. (*a*) Log-layer measured drag change for six riblet shapes, with a quadratic best fit of the dataset $\Delta U_{fit}^+$ forced to $\Delta U^+ = 0$ at $\ell_g^+ = 0$; adapted from Wong *et al.* (2024). (*b*) The corresponding turbulence origins $\ell_T^+ = \Delta U_{fit}^+ + h_\parallel^+$ (solid curves) which are applied in the linear-stability analysis; $h_\parallel^+$ being known for a given riblet shape. The symbols are $\ell_T^+ = \Delta U^+ + h_\parallel^+$ based on the DNS-measured $\Delta U^+$. (*c*) A comparison between *a priori* $\ell_T^+$ predictions with a viscous model (Wong *et al.* 2024) and $\ell_T^+ = \Delta U^+ + h_\parallel^+$ based on DNS measurements. Disagreement is not unexpectedly observed in the $\ell_g^+ \gtrsim 10$ region of interest.

displacement), could be accurately measured for large riblets in minimal-channel DNS (Chen & García-Mayoral 2023).

One option is to employ *a priori* predictions of $\ell_T^+$, e.g. the viscous vortex model predictions of Wong *et al.* (2024), which are accurate for smooth-wall-like riblets of sizes $\ell_g^+ \lesssim 10$, and which could be extrapolated to larger $\ell_g^+$. However, these *a priori* predictions of $\ell_T^+$ assume viscous in-groove flow, and become inaccurate for $\ell_g^+ \gtrsim 10$ for the very reason that spanwise rollers and other texture-coherent structures begin to appear (Modesti *et al.* 2021). By carrying additional Reynolds stresses and altering momentum transfer, these structures modify $\ell_T^+$, for which no accurate *a priori* predictions then exist. For the same reason, for $\ell_g^+ \gtrsim 10$, the concept of a smooth-wall-like turbulence origin $\ell_T^+$ breaks down, and a zero-plane displacement $d^+$ is defined in its place (Chen & García-Mayoral 2023).

However, the usefulness of a (viscous) smooth-wall-like approximation need not end at the limit of the viscous regime ($\ell_g^+ \lesssim 10$). For smooth-wall-like riblets with $\ell_g^+ \lesssim 10$, the drag reduction $\Delta U^+$ is $\approxeq -(\ell_U^+ - \ell_T^+)$ (Wong *et al.* 2024), and furthermore, from the cancellation in $\ell_U^+$ and $\ell_T^+$, the resulting magnitude of $\Delta U^+$ is typically an order of magnitude lower than that of $\ell_T^+$. Thus, for example, a large relative error in $\Delta U^+$ would correspond to a small relative error in $\ell_T^+$. Equally, when rollers and other drag-increasing mechanisms for riblets are weak, e.g. for $10 \lesssim \ell_g^+ \lesssim 20$, their contribution to $\Delta U^+$ may be of the order of $\Delta U^+$ (although certainly not an error), and yet this contribution may remain a small fraction of $\ell_T^+$, e.g. conservatively $\lesssim 20\,\%$ to $30\,\%$ for $\ell_g^+ \approx 20$, depending on the riblet shape. This provides a gauge of the relative error in $\ell_T^+$ if using a smooth-wall-like approximation $\Delta U^+ \approxeq -(\ell_U^+ - \ell_T^+)$ beyond its regime of applicability, noting that $\ell_T^+$ is the quantity of interest for roller predictions.

To obtain somewhat *a priori* predictions, $\Delta U^+$ values measured *a posteriori* from the DNS for all six riblet shapes considered herein are fit to a quadratic polynomial,

| Riblet cross-section | DNS-fitted $d^+ \approx \ell_T^+$ $c_1\ell_g^2 + (c_2 + (h_\parallel/\ell_g))\ell_g$ | *A priori* $\ell_T^+$ (Wong *et al.* 2024) $m_T\ell_g^2 + (h_\perp/\ell_g)\ell_g$ | Roller observations |
|---|---|---|---|
|  | $0.0092\ell_g^{+2} + (-0.17 + 0.20)\ell_g^+$ | $0.0010\ell_g^{+2} + 0.085\ell_g^+$ | Common |
|  | $0.0092\ell_g^{+2} + (-0.17 + 0.18)\ell_g^+$ | $0.0017\ell_g^{+2} + 0.076\ell_g^+$ | Common |
|  | $0.0092\ell_g^{+2} + (-0.17 + 0.26)\ell_g^+$ | $0.0026\ell_g^{+2} + 0.122\ell_g^+$ | Uncommon |
|  | $0.0092\ell_g^{+2} + (-0.17 + 0.29)\ell_g^+$ | $0.0028\ell_g^{+2} + 0.124\ell_g^+$ | Uncommon |
|  | $0.0092\ell_g^{+2} + (-0.17 + 0.25)\ell_g^+$ | $0.0030\ell_g^{+2} + 0.147\ell_g^+$ | Absent |
|  | $0.0092\ell_g^{+2} + (-0.17 + 0.28)\ell_g^+$ | $0.0041\ell_g^{+2} + 0.156\ell_g^+$ | Absent |

Table 2. Polynomial expressions for the turbulence origin $\ell_T^+$, from DNS-fitted $\Delta U^+$, and from *a priori* $\ell_T^+$ predictions (Wong *et al.* 2024), for each riblet shape. Whether spanwise rollers are observed in DNS (García-Mayoral & Jiménez 2011*b*; Endrikat *et al.* 2021*a*) for each riblet shape is also listed. Note that for the DNS-fits, $c_1$ and $c_2$ are intentionally identical for all riblets, as they are obtained from a single best fit of $\Delta U^+$ (figure 12*a*). Only $h_\parallel/\ell_g$ varies with riblet shape. The rows of this table are ordered by the value of $m_T$ from the *a priori* $\ell_T^+$ predictions (Wong *et al.* 2024), which correlates reasonably well with the likelihood of rollers (low $m_T$ indicating the highest likelihood of rollers and where $h_\perp$ is the spanwise protrusion height).

forced to zero at $\ell_g^+ = 0$. This best fit, as shown in figure 12(*a*), no longer depends on a specific riblet shape, and can be converted into an equivalent $\ell_T^+$ specific to a riblet shape through the smooth-wall-like approximation $\Delta U^+ \approxeq -(\ell_U^+ - \ell_T^+)$. Note that $\ell_U^+$ can be accurately predicted *a priori* from a routine Stokes-flow calculation of the streamwise protrusion height $h_\parallel^+$, as described in Luchini *et al.* (1991), up to $\ell_g^+ \approx 20$ (Wong *et al.* 2024), to well within a $\lesssim 20\,\%$ to $30\,\%$ relative error. The resulting riblet-specific $\ell_T^+ = \Delta U_{fit}^+ + h_\parallel^+$ values are then shown in figure 12(*b*), where the coloured lines are based on the best-fit $\Delta U^+$ from figure 12(*a*), and the coloured markers are from the riblet-specific measurements of $\Delta U^+ + h_\parallel^+$. The differences between the lines and the markers are then the differences between the fitted and measured $\Delta U^+$, again reinforcing that a large relative error in $\Delta U^+$ appears as a small relative error in $\ell_T^+$ (the error in figure 12*b* being between fitted and measured $\Delta U^+$). Thus, DNS-fitted $\ell_T^+$ are used throughout the entirety of the work, whenever relevant to the 2-D or 1-D linear-stability analysis, or the DNS post-processing (i.e. plotting spectra at $z^+ + \ell_T^+$), unless stated otherwise, and noting that in figure 4(*d*) growth rates based on DNS-matched $\ell_T^+$ (symbols in figure 12*b*) were compared with those with DNS-fitted $\ell_T^+$ (curves in figure 12*b*). *A priori* values of $\ell_U^+ = h_\parallel^+$ are also assumed throughout. For convenience, the polynomial expressions for the DNS-fitted $\ell_T^+$ values are provided in table 2, noting that the fitting coefficients $c_1$ and $c_2$ do not depend on the riblet shape, allowing for (approximately) *a priori* predictions of whether riblets will sustain rollers.

For reference, the viscous predictions of $\ell_T^+$ from Wong *et al.* (2024) are also compared with the DNS-matched $\ell_T^+$ values in figure 12(*c*). Although the viscous predictions of $\ell_T^+$ (dashed lines) deviate from the DNS-matched $\ell_T^+$ values (markers) for $\ell_g^+ \gtrsim 10$, the deviations give some indication of which riblets are likely to sustain rollers. The blade  and 30° triangular  riblets depart sharply from the viscous predictions, and the slopes of the $\ell_T^+$ trends with $\ell_g^+$ are especially shallow for these riblets. Moreover, expressing the viscous predictions of $\ell_T^+$ from Wong *et al.* (2024) in the form of their equation (4.9), the $m_T$ coefficient of the term quadratic in $\ell_g^+$ correlates reasonably well with the likelihood of rollers for a given riblet shape. Note that the rows of table 2

have been ordered by increasing $m_T$, and for each riblet shape, the likelihood of roller observations listed based on previous DNS (Endrikat *et al.* 2021*a*,*b*). Physically, small values of $m_T$ represent reduced wall-normal transpiration at the riblet crests (Wong *et al.* 2024), i.e. momentum transfer between the in-groove and overlying flow is limited. This reduced transpiration (reduced $m_T$) for some riblet shapes leads to a more uniform in-groove flow, which provides a stronger mixing layer. Thus, even viscous predictions afford some guidance as to whether riblets are likely to sustain rollers; 2-D linear-stability analysis results with viscous vortex $\ell_T^+$ values were also discussed in § 3.2.

## Appendix D. Comparison between linear-stability analysis and resolvent analysis and the sensitivity of the roller mode

The wall-admittance boundary condition (4.2) is applied in the resolvent framework (McKeon & Sharma 2010; Luhar *et al.* 2015; Chavarin *et al.* 2021) to rule out the resolvent forcing as an explanation for previously observed differences in roller modes from linear-stability and resolvent analysis, as discussed in §§ 2 and 3. This 1-D analysis shows that the high-relative-gain roller modes identified in resolvent analysis (Chavarin & Luhar 2020; Chavarin *et al.* 2021) are no more than marginal roller modes, explaining why differences between linear-stability and resolvent analysis were observed only when assuming rollers were a maximally growing instability (García-Mayoral & Jiménez 2011*b*; Gómez-de-Segura *et al.* 2018*b*). In particular, the spanwise-infinite modes only maximise the gain of the first singular value of the resolvent operator as the rollers approach marginal stability, i.e. there is good agreement between the results of figure 13(*a*) and those of the inset of figure 13(*b*). Thus, previous detections of roller modes in the resolvent framework serve to provide complementary insights into the dynamics of rollers over riblets (Chavarin & Luhar 2020) and anisotropic permeable substrates (Chavarin *et al.* 2021). In addition, the good agreement between the linear-stability and resolvent analyses further indicates that the dynamics of the spanwise rollers are primarily modal, and that other sources of non-modal amplification inherent in the white-noise resolvent forcing (Symon *et al.* 2018) are unlikely to dictate the dynamics of spanwise rollers.

The sensitivity of the spanwise wavelength of the roller mode is further considered in figure 14, for various model boundary conditions (either uniform, $\kappa_x^+$ or $\kappa_x^{+2}$ amplitude dependence, and either 180°, 250° or 270° phase.) In particular, note that the wavelength for marginal stability (solid markers in the bottom row of figure 14) varies significantly with the choice of model boundary condition (and with a uniform wall admittance, occurs at $\lambda_x^+ > 10^3$ for two of the admittance phases considered). Overall, this sensitivity in the streamwise wavelength dynamically demonstrates the importance of accurately capturing the in-groove dynamics with the appropriate effective boundary condition (e.g. purely pressure–viscous with $\kappa_x^{+2}$ amplitude dependence and 180° phase, vs pressure–unsteady-inertia with $\kappa_x^+$ amplitude dependence and 270° phase, or somewhere between). Overall, this sensitivity to the boundary condition further motivates the use of riblet-resolving simulations, to ensure that the correct physical balance within the grooves is captured in any ensuing 1-D analysis.

## Appendix E. Linear-stability analysis about either DNS or Cess mean flows

In this section, various mean-flow approximations are compared in the linear-stability analysis.

First, results with riblet-resolved 2-D mean profiles (Cess eddy-viscosity shifted by fitted-$\ell_T^+$) are compared with results with $x$-$t$-riblet-averaged DNS mean profiles in

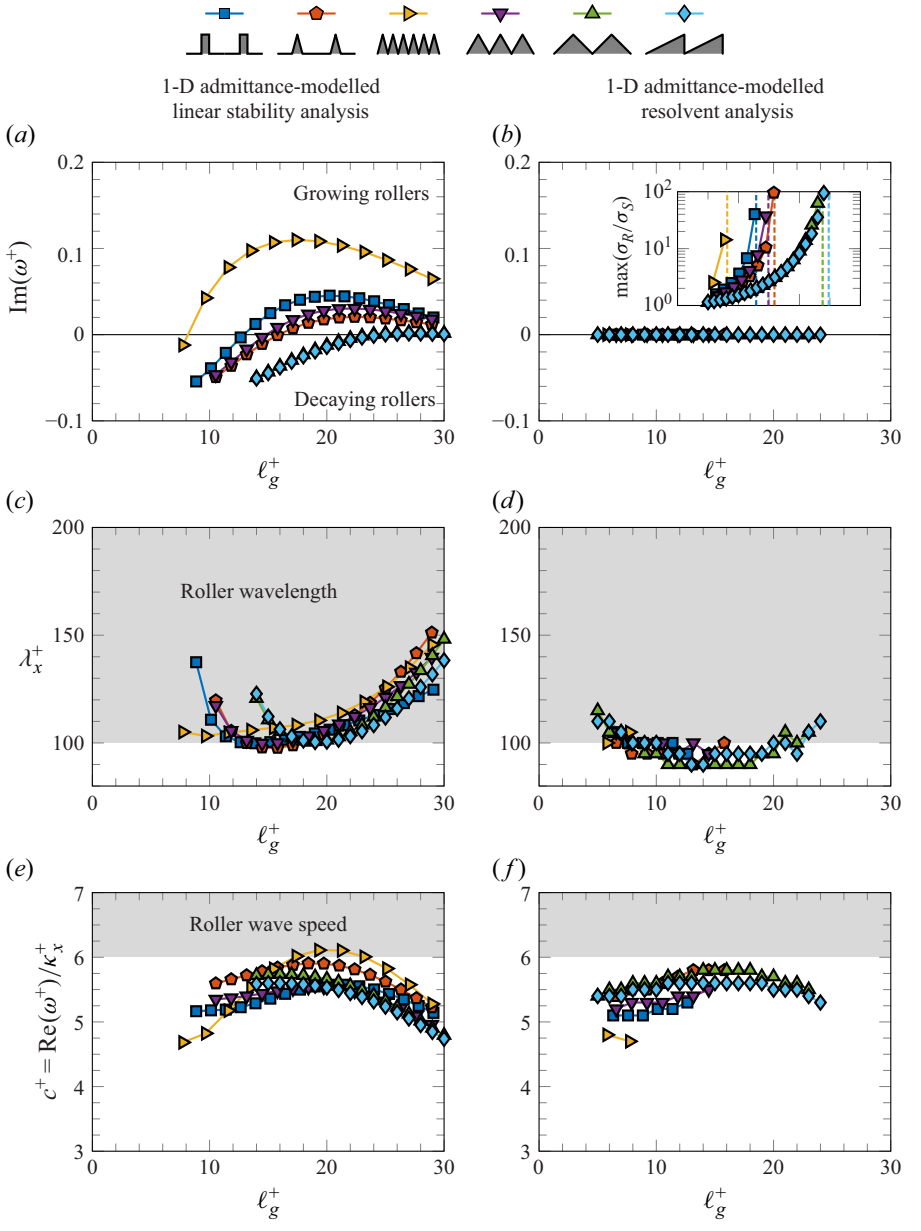


Figure 13. Comparing 1-D linear stability and 1-D resolvent analysis with identical modelled boundary conditions. The 1-D wall-admittance boundary conditions are $\hat{w}^+/\hat{p}^+ = (A^+_{g,-\ell_U}/s^+)(\kappa_x^+/6)\exp(250\pi\mathrm{i}/180)$ and $\hat{u}^+ = 0$ at $z^+ = -\ell_U^+$, with superficially averaged mean-velocity profiles obtained from riblet-resolved 2-D calculations for each riblet size. Note that the inset in (*b*) provides the relative gain of the leading resolvent mode, which consistently increases as the roller mode approaches marginal stability (the dashed lines indicate the $\ell_g^+$ at which positive growth rates are first attained in the 1-D linear-stability analysis, and which indicate good agreement between the two approaches), and where $\sigma_R$ and $\sigma_S$ are the gain of the leading resolvent modes for riblets and a smooth wall, respectively.

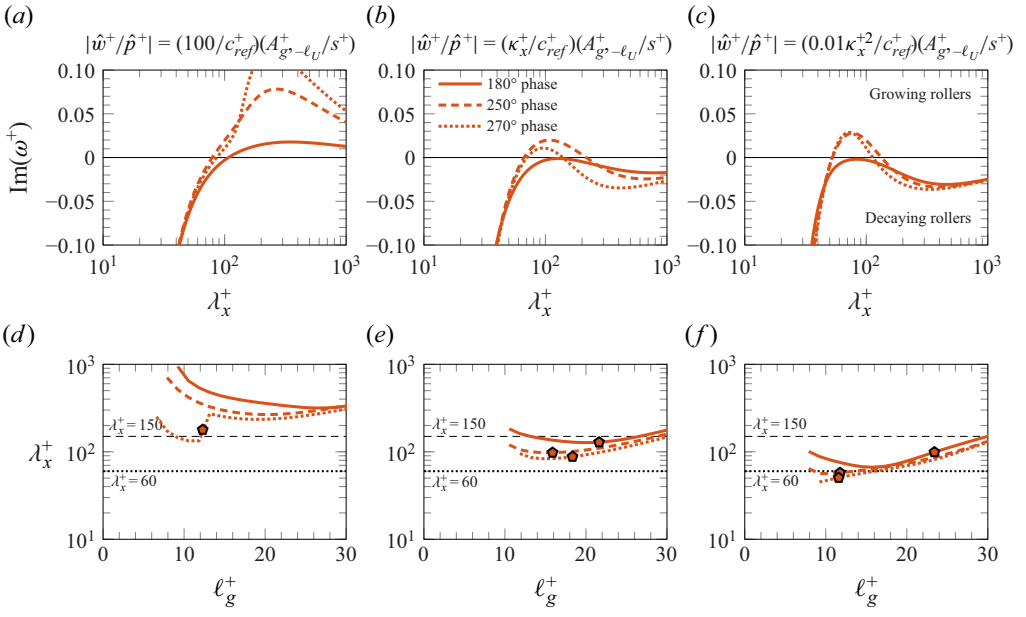


Figure 14. Testing modified forms of the effective wall-admittance boundary condition, specifically, three different scale dependences for the admittance amplitude, and three different phases. Not all amplitude-scale dependence and phase relations are necessarily achievable from a manufactured surface. (*a–c*) Fixed riblet size ($\ell_g^+ \approx 20$ trapezoids), plotting the growth rate across streamwise wavelengths. (*d–f*) Streamwise wavelength for peak growth, across $\ell_g^+$ (trapezoids). Solid markers indicate the wavelength at the point of marginal stability, for each of the admittance amplitude and phase combinations tested (two marginal wavelengths with a uniform wall-admittance amplitude exceeded $\lambda_x^+ = 10^3$, so are not plotted).

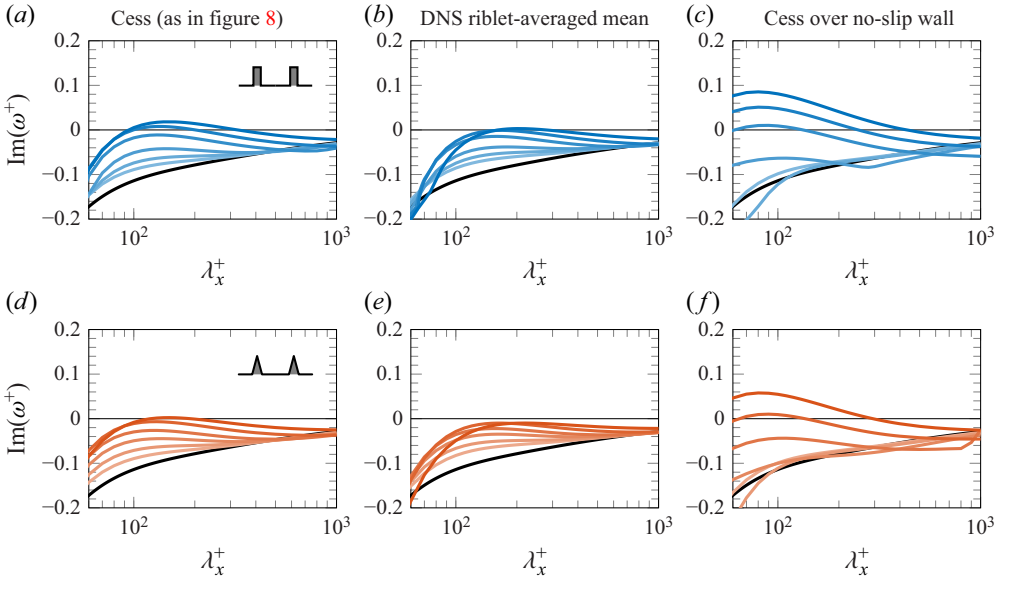


Figure 15. Comparing the growth rates predicted with the riblet-resolved 2-D mean flows with Cess eddy-viscosity shifted by $\ell_T^+$ (left column) to their DNS equivalents (middle column), and to the use of 1-D mean flows over a no-slip wall (right column; with Cess shifted by the same $\ell_T^+$). In all cases the perturbations experience no-slip riblets. The riblet-resolved 2-D mean flows provide predictions consistent with DNS, while predictions with 1-D mean flows over no-slip walls are not.

figure 15 (left, middle columns). As shown, the riblet-resolved 2-D profiles (left column) provide predictions consistent with the DNS mean profiles (middle column) for all riblet shapes tested. Prediction accuracy is affected by both the choice of $\ell_T^+$ and the use of an eddy-viscosity closure, although neither approximation leads to predictions overly inconsistent with those from the DNS.

Second, results with riblet-resolved 2-D mean profiles are compared with results with mean profiles over a no-slip wall in figure 15 (middle, right columns), i.e. comparing results based on the same shifted eddy-viscosity profile applied over either riblets or a no-slip wall, while the perturbations still experience no-slip riblets. The use of mean profiles over a no-slip wall (right column) leads to predictions which are inconsistent with those based on the riblet-resolved DNS profiles (middle column), unlike when the same shifted eddy-viscosity profile is applied over riblets (left column). Thus, 1-D mean flows obtained over a no-slip wall should be treated with caution in any 1-D analysis with an effective boundary condition.

Third, results with riblet-resolved 2-D mean profiles are compared with results with intrinsically averaged mean profiles in figure 16. For reference, the superficial and intrinsic spanwise averages of $U$ are

$$\langle U(z)\rangle_y\big|_{superficial} = \frac{1}{s}\int_{t_r(z)/2}^{s-t_r(z)/2} U(y,z)\,\mathrm{d}y \tag{E1}$$

and

$$\langle U(z)\rangle_y\big|_{intrinsic} = \frac{s}{s-t_r(z)}\langle U(z)\rangle_y\big|_{superficial}\,, \tag{E2}$$

respectively, where $t_r$ is the thickness of the (symmetric) riblet as a function of wall-normal height. Note that the superficial average provides, for example, an effective boundary condition applicable across an entire wall-normal slice (i.e. across 0 to $s$, at fixed $z^+ = -\ell_U^+$), rather than representing the effective boundary condition across only the fluid region. As shown in figure 16, results with intrinsically averaged mean profiles (right column) remain consistent with both predictions based on the DNS mean profiles (middle column) and riblet-resolved 2-D mean profiles (left column). However, the 1-D analysis (§ 5) predicted that all sufficiently large riblets would generate spanwise rollers, at odds with DNS observations (§ 2) and the 2-D linear-stability analysis. Rollers do not appear when the perturbations experience no-slip riblets with either 2-D or intrinsically averaged (1-D) mean flows, for both 90° triangular  and asymmetric triangular  riblets for all $\ell_g^+$ tested. This result thereby suggests that improvements to the boundary condition applied in the 1-D analysis are required for very large $\ell_g^+ \gtrsim 20$ riblets, as a spanwise-uniform mean-flow approximation is yet to completely break down (although spanwise variations become relevant at smaller $\ell_g^+$ values for less-slender riblets).

These comparisons (figures 15 and 16) again reinforce the importance of capturing the mean-flow details within the riblet grooves, even in a spanwise-averaged sense. The key differences between the mean-flow approximations, i.e. no-slip wall shifted-Cess vs riblet-resolved shifted-Cess or DNS, appear near the riblet crests. In particular, with no-slip wall shifted-Cess, $\partial_z U^+ = 1$ between $z^+ = -\ell_T^+$ and $z^+ = -\ell_U^+$, unlike with the superficially averaged 2-D profiles, where $\partial_z\langle U^+\rangle_y$ noticeably reduces throughout the upper portion of the riblet grooves.

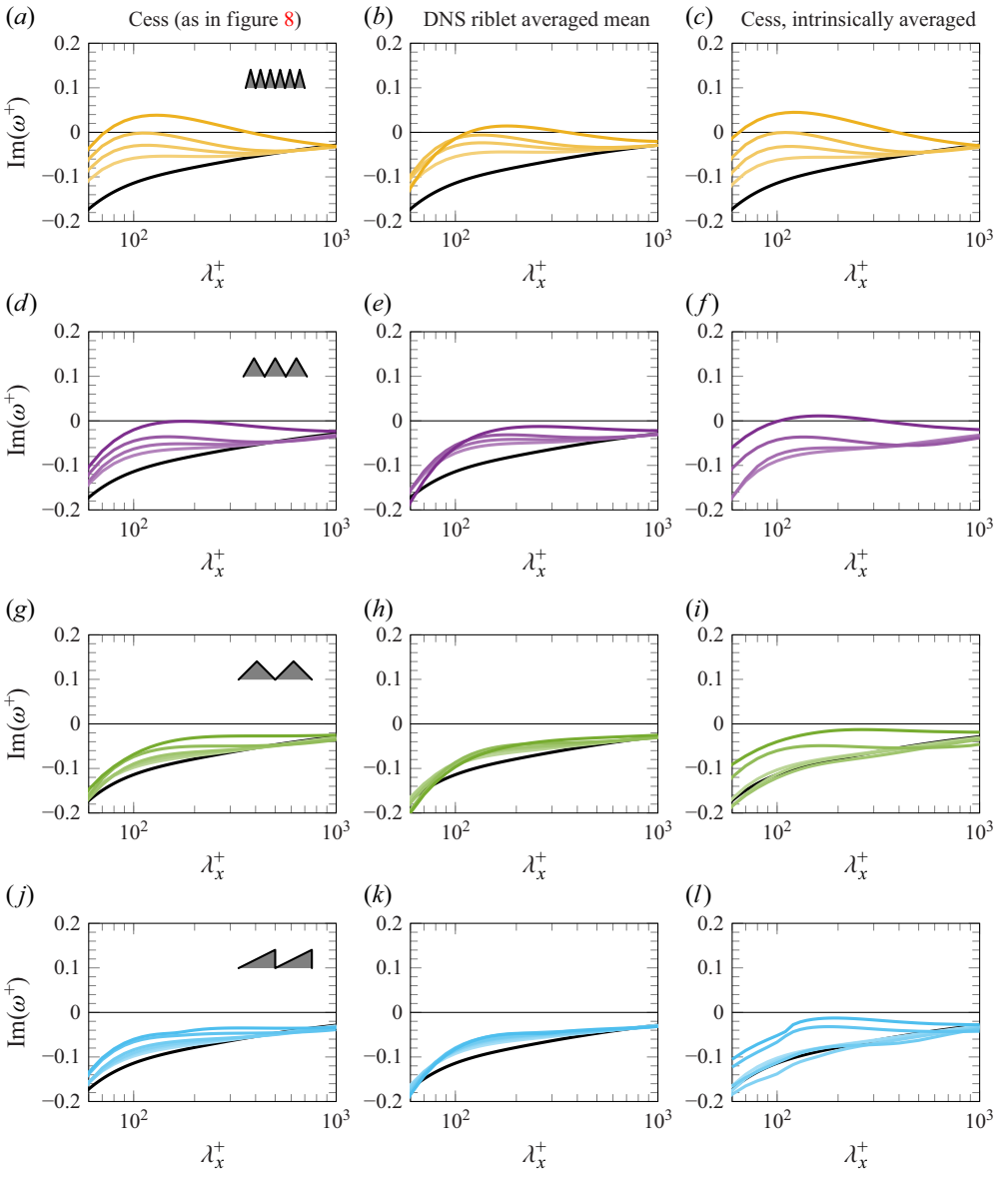


Figure 16. Comparing the growth rates predicted with the riblet-resolved 2-D mean flows (left column) to their DNS equivalents (middle column), and to predictions with the intrinsic averages of the riblet-resolved 2-D mean flows (right column). Decaying rollers are still predicted when employing the spanwise-uniform intrinsic averages for the least slender of the triangular riblets, although only just. Thus, the approximation of a 1-D mean flow is yet to completely break down.

## Appendix F. Detailed comparison between the 2-D and 1-D eigenmodes

The validity of the 1-D analysis, and specifically the chosen boundary conditions, i.e. wall-admittance boundary condition (4.2) with a no-slip condition on streamwise velocity, is qualitatively assessed by comparing the leading eigenmodes from the 1-D and 2-D analysis for trapezoidal riblets in figure 17. As shown, the pressure (figure 17, right column) remains highly uniform across the entire span, regardless of the presence of the riblets, and so the 1-D and 2-D eigenmodes look almost identical. The wall-normal velocity

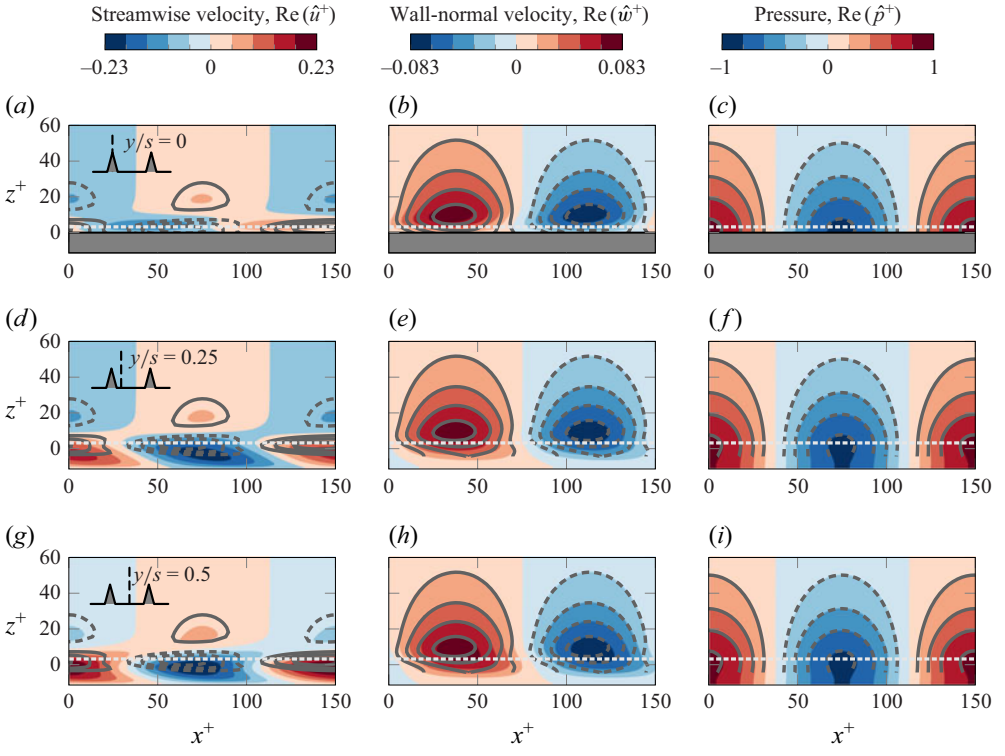


Figure 17. Comparing the real parts of the leading eigenmode from the 1-D linear-stability analysis (solid/dashed lines) and the 2-D analysis (coloured contours). Columns are streamwise velocity, wall-normal velocity and pressure, respectively. Across different spanwise locations (rows), there remains good agreement between the 1-D and 2-D modes in the pressure perturbations, while for the wall-normal velocity, there are some slight differences, particularly near the riblet crests. The largest differences are observed in the streamwise velocity, although some resemblance is still maintained. Note that the domain for the 1-D linear-stability analysis extends only to $z^+ = -\ell_U^+$, and not to the valley floor at $z^+ = -k^+$. The dashed off-white lines indicate the local minimum in $\partial_{zz}U^+$.

(figure 17, middle column) also maintains a reasonable degree of spanwise uniformity, with only slight variations at spanwise slices near the riblets, and with spanwise variations absent once a few viscous units above the riblet crests. The overall good agreement in the wall-normal velocity and pressure contours between the 1-D and 2-D eigenmodes further supports the use of the wall-admittance boundary condition (4.2) in the 1-D analysis. These observations are also qualitatively similar to those from DNS (García-Mayoral & Jiménez 2011*b*; Endrikat *et al.* 2021*a*), where the rollers remain coherent across multiple riblet spacings, in spite of slight disruptions in the wall-normal velocity near the individual riblets (e.g. comparing figures 17*b* and 17*e*). However, larger differences between the 2-D and 1-D modes are observed in the streamwise velocity (figure 17, left column), and suggest that the imposition of a no-slip condition on the streamwise velocity should be relaxed, for larger riblets especially. However, applying $\hat{u}^+ = 0$ in concert with the wall-admittance boundary condition (4.2) still provides reasonable predictions for roller-promoting riblets with $\ell_g^+ \lesssim 20$, allowing many of the key features of the 2-D roller modes to be captured in the 1-D analysis.

The influence of the riblet size and shape on the spanwise rollers is also made apparent through the localisation of the roller mode. Specifically, the rollers tend to localise where

$\partial_{zz}U^+$ is a minimum, as $\partial_{zz}U^+$ here drives perturbation energy production (Jiménez *et al.* 2001; García-Mayoral & Jiménez 2011*b*; McKeon 2017). For these $\ell_g^+ \approx 15$ trapezoidal riblets, the minimum in $\partial_{zz}U^+$ is approximately 3 viscous units above the riblet crests (dashed off-white lines in figure 17), about which the streamwise velocity contours in particular tend to localise (the heads of the wall-normal velocity modes sit slightly above this location). Thus, the shear-layer height is approximately 7 viscous units, as the DNS-interpolated $\ell_T^+$ for these riblets is approximately 4 units below the crests. This shear-layer height is approximately unchanged from that over a smooth wall, and equally sets the wave speed of the roller mode, as $c^+ \approx U^+ \approx 7$ (García-Mayoral & Jiménez 2011*b*). As the shear-layer height is approximately unchanged percentage-wise, it is instead the localisation of the roller mode about the minimum in $\partial_{zz}U^+$ that explains much of the sensitivity to $\ell_T^+$, as observed in the roller growth rate and wave-speed predictions (recalling figure 4). Small changes to $\ell_T^+$, of 1 to 2 viscous units, lead to commensurate changes in how far above the riblet crests the roller modes localise, thereby influencing the growth rates and wave speeds. It is only the overall wall-normal extent of the roller modes ($\approx 50$ viscous units), that has little dependence on $\ell_T^+$.

## References


Abu Rowin, W., Deshpande, R., Wang, S., Kozul, M., Chung, D., Sandberg, R.D. & Hutchins, N. 2025 Experimental characterisation of Kelvin–Helmholtz rollers over riblet surfaces. *J. Fluid Mech.* **1009**, A65.

Bottaro, A. 2019 Flow over natural or engineered surfaces: an adjoint homogenization perspective. *J. Fluid Mech.* **877**, P1.

Bottaro, A. & Naqvi, S.B. 2020 Effective boundary conditions at a rough wall: a high-order homogenization approach. *Meccanica* **55**, 1781–1800.

Breugem, W.P., Boersma, B.J. & Uittenbogaard, R.E. 2006 The influence of wall permeability on turbulent channel flow. *J. Fluid Mech.* **562**, 35–72.

Brooke Benjamin, T. 1960 Effects of a flexible boundary on hydrodynamic stability. *J. Fluid Mech.* **9** (4), 513–532.

Carpenter, P.W. & Garrad, A.D. 1986 The hydrodynamic stability of flow over Kramer-type compliant surfaces. Part 2. Flow-induced surface instabilities. *J. Fluid Mech.* **170**, 199–232.

Chan, L., Kevin, Skvortsov, A. & Ooi, A. 2023 Effect of straight riblets on the underlying surface on wall bounded flow drag. *Intl J. Heat Fluid Flow* **102**, 109160.

Chavarin, A., Gómez-de-Segura, G., García-Mayoral, R. & Luhar, M. 2021 Resolvent-based predictions for turbulent flow over anisotropic permeable substrates. *J. Fluid Mech.* **913**, A24.

Chavarin, A. & Luhar, M. 2020 Resolvent analysis for turbulent channel flow with riblets. *AIAA J.* **58** (2), 589–599.

Chen, Z. & García-Mayoral, R. 2023 Examination of outer-layer similarity in wall turbulence over obstructing surfaces. *J. Fluid Mech.* **973**, A31.

Chu, D.C. & Karniadakis, G.E. 1993 A direct numerical simulation of laminar and turbulent flow over riblet-mounted surfaces. *J. Fluid Mech.* **250**, 1–42.

Chu, X., Yang, G., Pandey, S. & Weigand, B. 2019 Direct numerical simulation of convective heat transfer in porous media. *Intl J. Heat Mass Transfer* **133**, 11–20.

Drazin, P.G. & Reid, W.H. 2004 *Hydrodynamic Stability*. Cambridge University Press.

Endrikat, S., Modesti, D., García-Mayoral, R., Hutchins, N. & Chung, D. 2021*a* Influence of riblet shapes on the occurrence of Kelvin–Helmholtz rollers. *J. Fluid Mech.* **913**, A37.

Endrikat, S., Modesti, D., MacDonald, M., García-Mayoral, R., Hutchins, N. & Chung, D. 2021*b* Direct numerical simulations of turbulent flow over various riblet shapes in minimal-span channels. *Flow Turbul. Combust.* **107**, 1–29.

Endrikat, S., Newton, R., Modesti, D., García-Mayoral, R., Hutchins, N. & Chung, D. 2022 Reorganisation of turbulence by large and spanwise-varying riblets. *J. Fluid Mech.* **952**, A27.

Finnigan, J. 2000 Turbulence in plant canopies. *Annu. Rev. Fluid Mech.* **32**, 519–571.

García-Mayoral, R. & Jiménez, J. 2011*a* Drag reduction by riblets. *Phil. Trans. R. Soc. Lond. A* **369**, 1412–1427.

García-Mayoral, R. & Jiménez, J. 2011*b* Hydrodynamic stability and breakdown of the viscous regime over riblets. *J. Fluid Mech.* **678**, 317–347.
García-Mayoral, R. & Jiménez, J. 2012 Scaling of turbulent structures in riblet channels up to $Re_\tau \approx 550$. *Phys. Fluids* **24** (10), 105101.
Geuzaine, C. & Remacle, J.-F. 2009 Gmsh: a three-dimensional finite element mesh generator with built-in pre- and post-processing facilities. *Intl J. Numer. Meth. Engng* **79** (11), 1309–1331.
Ghisalberti, M. 2009 Obstructed shear flows: similarities across systems and scales. *J. Fluid Mech.* **641**, 51–61.
Goldstein, D., Handler, R. & Sirovich, L. 1995 Direct numerical simulation of turbulent flow over a modelled riblet covered surface. *J. Fluid Mech.* **302**, 333–376.
Gómez-de-Segura, G. 2019 Turbulent drag reduction by anisotropic permeable substrates. PhD thesis, University of Cambridge, Cambridge, UK.
Gómez-de-Segura, G., Fairhall, C.T., MacDonald, M., Chung, D. & García-Mayoral, R. 2018*a* Manipulation of near-wall turbulence by surface slip and permeability. *J. Phys.: Conf. Ser.* **1001**, 012001.
Gómez-de-Segura, G. & García-Mayoral, R. 2019 Turbulent drag reduction by anisotropic permeable substrates–analysis and direct numerical simulations. *J. Fluid Mech.* **875**, 124–172.
Gómez-de-Segura, G. & García-Mayoral, R. 2020 Imposing virtual origins on the velocity components in direct numerical simulations. *Intl J. Heat Fluid Flow* **86**, 108675.
Gómez-de-Segura, G., Sharma, A. & García-Mayoral, R. 2018*b* Turbulent drag reduction using anisotropic permeable substrates. *Flow Turbul. Combust.* **100** (4), 995–1014.
Habibi Khorasani, S.M., Lacis, U., Pasche, S., Rosti, M.E. & Bagheri, S. 2022 Near-wall turbulence alteration with the transpiration-resistance model. *J. Fluid Mech.* **942**, A45.
Habibi Khorasani, S.M., Luhar, M. & Bagheri, S. 2024 Turbulent flows over porous lattices: alteration of near-wall turbulence and pore-flow amplitude modulation. *J. Fluid Mech.* **984**, A63.
Hao, Z. & García-Mayoral, R. 2025 Turbulent flows over porous and rough substrates. *J. Fluid Mech.* **1008**, A1.
Hartog, F.H., van Nesselrooij, M., van Campenhout, O.W.G., Schrijer, F.F.J., van Oudheusden, B.W. & Masania, K. 2024 Turbulent boundary layers over substrates with streamwise-preferential permeability. *Phys. Rev. Fluids* **9** (11), 114602.
Hecht, F. 2012 New development in FreeFem++. *J. Numer. Maths* **20** (3-4), 251–266.
Jiménez, J., Uhlmann, M., Pinelli, A. & Kawahara, G. 2001 Turbulent shear flow over active and passive porous surfaces. *J. Fluid Mech.* **442**, 89–117.
Kuwata, Y. 2022 Role of spanwise rollers by Kelvin–Helmholtz instability in turbulence over a permeable porous wall. *Phys. Rev. Fluids* **7** (8), 084606.
Lacis, U. & Bagheri, S. 2017 A framework for computing effective boundary conditions at the interface between free fluid and a porous medium. *J. Fluid Mech.* **812**, 866–889.
Lacis, U., Sudhakar, Y., Pasche, S., Rosti, M.E. & Bagheri, S. 2020 Transfer of mass and momentum at rough and porous surfaces. *J. Fluid Mech.* **884**, A21.
Landahl, M.T. 1962 On the stability of a laminar incompressible boundary layer over a flexible surface. *J. Fluid Mech.* **13** (4), 609–632.
Luchini, P. 2013 Linearized no-slip boundary conditions at a rough surface. *J. Fluid Mech.* **737**, 349–367.
Luchini, P., Manzo, F. & Pozzi, A. 1991 Resistance of a grooved surface to parallel flow and cross-flow. *J. Fluid Mech.* **228**, 87–109.
Luhar, M., Sharma, A.S. & McKeon, B.J. 2014 Opposition control within the resolvent analysis framework. *J. Fluid Mech.* **749**, 597–626.
Luhar, M., Sharma, A.S. & McKeon, B.J. 2015 A framework for studying the effect of compliant surfaces on wall turbulence. *J. Fluid Mech.* **768**, 415–441.
MacDonald, M., Chan, L., Chung, D., Hutchins, N. & Ooi, A. 2016 Turbulent flow over transitionally rough surfaces with varying roughness densities. *J. Fluid Mech.* **804**, 130–161.
MacDonald, M., Chung, D., Hutchins, N., Chan, L., Ooi, A. & García-Mayoral, R. 2017 The minimal-span channel for rough-wall turbulent flows. *J. Fluid Mech.* **816**, 5–42.
McKeon, B.J. 2017 The engine behind (wall) turbulence: perspectives on scale interactions. *J. Fluid Mech.* **817**, P1.
McKeon, B.J. & Sharma, A.S. 2010 A critical-layer framework for turbulent pipe flow. *J. Fluid Mech.* **658**, 336–382.
Mele, B., Saetta, E. & Tognaccini, R. 2023 Analysis of riblets modeling for aeronautical applications. *AIAA Scitech 2023 Forum*, 2023-3748.
Mele, B., Tognaccini, R., Catalano, P. & de Rosa, D. 2020 Effect of body shape on riblets performance. *Phys. Rev. Fluids* **5**, 124609.

MOARREF, R. & JOVANOVIĆ, M.R. 2012 Model-based design of transverse wall oscillations for turbulent drag reduction. *J. Fluid Mech.* **707**, 205–240.
MODESTI, D., ENDRIKAT, S., HUTCHINS, N. & CHUNG, D. 2021 Dispersive stresses in turbulent flow over riblets. *J. Fluid Mech.* **917**, A55.
MOTOKI, S., TSUGAWA, K., SHIMIZU, M. & KAWAHARA, G. 2022 The ultimate state of turbulent permeable-channel flow. *J. Fluid Mech.* **931**, R3.
NAQVI, S.B. & BOTTARO, A. 2021 Interfacial conditions between a free-fluid region and a porous medium. *Intl J. Multiphase Flow* **141**, 103585.
NEPF, H., GHISALBERTI, M., WHITE, B. & MURPHY, E. 2007 Retention time and dispersion associated with submerged aquatic canopies. *Water Resour. Res.* **43** (4), W04422.
NEPF, H.M. 2012 Flow and transport in regions with aquatic vegetation. *Water Resour. Res.* **44**, 123–142.
RAUPACH, M.R., FINNIGAN, J.J. & BRUNEI, Y. 1996 Coherent eddies and turbulence in vegetation canopies: the mixing-layer analogy. *Boundary-Layer Meteorol.* **78**, 351–382.
REYNOLDS, W.C. & TIEDERMAN, W.G. 1967 Stability of turbulent channel flow, with application to Malkus's theory. *J. Fluid Mech.* **27** (2), 253–272.
ROUHI, A., ENDRIKAT, S., MODESTI, D., SANDBERG, R.D., ODA, T., TANIMOTO, K., HUTCHINS, N. & CHUNG, D. 2022 Riblet-generated flow mechanisms that lead to local breaking of Reynolds analogy. *J. Fluid Mech.* **951**, A45.
SHAHZAD, H., HICKEL, S. & MODESTI, D. 2023 Turbulence and added drag over acoustic liners. *J. Fluid Mech.* **965**, A10.
SHARMA, A. & GARCÍA-MAYORAL, R. 2020 Turbulent flows over dense filament canopies. *J. Fluid Mech.* **888**, A2.
SUGA, K., OKAZAKI, Y., HO, U. & KUWATA, Y. 2018 Anisotropic wall permeability effects on turbulent channel flows. *J. Fluid Mech.* **855**, 983–1016.
SYMON, S., ROSENBERG, K., DAWSON, S.T.M. & MCKEON, B.J. 2018 Non-normality and classification of amplification mechanisms in stability and resolvent analysis. *Phys. Rev. Fluids* **3**, 053902.
VIGGIANO, B., CAMOBRECO, C.J., WONG, J., LUHAR, M., GARCÍA-MAYORAL, R., CHUNG, D. & GAYME, D. 2024 The role of nonlinear interactions in the onset of drag increase in flow over riblets. *J. Phys.: Conf. Ser.* **2753**, 012010.
WEIDEMAN, J.A.C. & REDDY, S.C. 2001 A MATLAB differentiation matrix suite. *ACM Trans. Math. Softw.* **26** (4), 465–519.
WONG, J., CAMOBRECO, C.J., GARCÍA-MAYORAL, R., HUTCHINS, N. & CHUNG, D. 2024 A viscous vortex model for predicting the drag reduction of riblet surfaces. *J. Fluid Mech.* **978**, A18.
ZAMPOGNA, G.A. & BOTTARO, A. 2016 Fluid flow over and through a regular bundle of rigid fibres. *J. Fluid Mech.* **792**, 5–35.